

Solar tower CSP plants with transcritical cycles based on CO₂ mixtures: A sensitivity on storage and power block layouts

Ettore Morosini^{*}, Enrico Villa, Guglielmo Quadrio, Marco Binotti, Giampaolo Manzolini

Politecnico di Milano, Dipartimento di Energia, Via Lambruschini 4, Milano 20156, Italy

ARTICLE INFO

Keywords:

CO₂ mixtures
Transcritical cycles
CSP applications
Power cycle analysis
Annual energy analysis

ABSTRACT

In this work three CO₂-based binary mixtures, CO₂ + C₆F₆, CO₂ + C₂H₃N and CO₂ + C₄F₈, are compared as innovative working fluids for closed power cycles in CSP plants. Adopted in transcritical cycles, they lead to cycle efficiencies higher than sCO₂ cycles at minimum temperatures above 50 °C, a typical condition for arid regions with high solar radiation. The analysis considers four plant configurations: the first with direct storage, solar salts as HTF and cycle maximum temperatures of 550 °C, while the three other plants adopt sodium as HTF and an indirect storage system, designed for cycle maximum temperatures of 550 °C, 625 °C and 700 °C. Detailed models are used to characterize the solar fields optical performance, the receiver thermal efficiency and the HTF pump consumption, both at design and off-design conditions, for large scale plants located in Las Vegas. Different power block layouts are considered, spanning from the more efficient ones to cycles with a high heat recovery capacity. In addition, the impact of the mixtures on the design of heat exchangers is evidenced, with convincing results with respect to the heat transfer characteristics of CO₂. Considering the resulting yearly performances and LCOE of each configuration, the adoption of indirect storage systems is considered a viable solution for high temperature solar plants. The three innovative mixtures allow for a reduction in LCOE with respect to sCO₂ cycles (up to 10 \$/MWh, depending on the configuration), capacity factors above 70% for the specific location, optimal solar multiples around 2.8 and 12 equivalent hours of TES.

1. Introduction

Concentrated solar power (CSP) is renowned as one of the most promising dispatchable renewable energy technologies to provide clean power to the grid. The most important peculiarity of CSP, in fact, is its native capability to include a thermal energy storage (TES) system to decouple the solar radiation availability to the actual electric power production, marking a decisive difference between CSP and other renewable energy technologies, as wind power or photovoltaic (PV), that have a wider diffusion and can, in the current scenario, enjoy much lower specific capital costs [1].

However, a limited number of large-scale CSP plants is nowadays in operation worldwide, with an overall electricity production around 14.5 TWhel in 2020 [2], 56 times lower than PV, in the same time span. CSP is penalized with respect to other renewable technologies both by its high financial costs (due to the perceived early-stage maturity of the technology itself [3] and by the modest net electric conversion efficiencies of the power blocks in operation, mainly based on steam cycle technology, with values around 35% for conventional parabolic through

system adopting synthetic oil as heat transfer fluid (HTF) and around 40% for the state-of-the-art solar tower systems using solar salts (60% NaNO₃, 40% KNO₃) as HTF [4].

As a matter of fact, solar tower systems are considered the most promising solutions for the next generation CSP plants, as they allow for high concentration ratios (easily above 1000) and therefore higher maximum temperatures of the HTF flowing in the receiver [5]. In addition, most of the research carried out within the last decade identifies in the next generation of CSP plants the capability of working with a maximum temperature of the power cycle around 700 °C adopting either sodium [6] or advanced solar salts as HTF or solid particles as heat transfer medium [7], since state-of-the-art solar salts are not thermally stable up to 700 °C.

In order to efficiently exploit the high temperatures reachable with next generation receivers, supercritical CO₂ power cycles (sCO₂) have been identified within the scientific community as a valid and viable solution in CSP configurations, with superior performance with respect to conventional steam Rankine cycles [8]: in fact, sCO₂ cycles can theoretically allow for cycle efficiencies up to 50% for large scale plants [9–11].

^{*} Corresponding author.

E-mail address: ettore.morosini@polimi.it (E. Morosini).

<https://doi.org/10.1016/j.solener.2023.05.054>

Received 24 January 2023; Received in revised form 15 May 2023; Accepted 27 May 2023

Available online 14 June 2023

0038-092X/© 2023 The Authors. Published by Elsevier Ltd on behalf of International Solar Energy Society. This is an open access article under the CC BY-NC-ND license (<http://creativecommons.org/licenses/by-nc-nd/4.0/>).

Nomenclature	
<i>Acronyms</i>	
A	Heat Exchange Area of the Heat Exchangers [m ²]
CAPEX	Capital Cost [\$]
CEPCI	Chemical Engineering Plant Cost Index
CF	Capacity Factor [%]
CSP	Concentrated Solar Power
DNI	Direct Normal Irradiation [W/m ²]
EoS	Equation of State
HTF	Heat Transfer Fluid
KPI	Key Performance Indicator
LC	Lethal Concentration [ppm/h]
LCOE	Levelized Cost of Electricity [\$/MWh]
OPEX	Operating Cost [\$]
ORC	Organic Rankine Cycle
PCHE	Printed Circuit Heat Exchanger
PHE	Primary Heat Exchanger
PV	Photovoltaic
SAM	System Advisory Model
sCO ₂	Supercritical Carbon Dioxide
S&T	Shell and Tubes Heat Exchanger
SM	Solar Multiple
TES	Thermal Energy Storage
U	Overall Heat Transfer Coefficient of a Heat Exchanger [W/m ² /K]
UA	Product between U and A of a Heat Exchanger
VLE	Vapour Liquid Equilibrium of a mixture
<i>Symbols</i>	
$\dot{Q}_{h,HTF}$	Thermal power transferred to the HTF (hourly average) [MW]
$\dot{Q}_{h,Receiver}$	Thermal power at the receiver (hourly average) [MW]
$\dot{Q}_{h,Sun}$	Thermal power recovered from the solar field (hourly average) referring to A_{SF} as collecting area [MW]
\dot{m}_{HTF}	Mass flow rate of the HTF (hourly average) [kg/s]
A_{SF}	Sum of the area of each heliostat on the solar field [m ²]
$D_{in,Tube}$	Internal diameter of the tube [m]
L_{tube}	Length of the tube [m]
N_{panels}	Number of panels for each flow path of the receiver
V_{HTF}	Velocity of the HTF [m/s]
$W_{Compression}$	Mechanical power absorbed by the compressor/pump of the cycle [MW]
$W_{Expansion}$	Mechanical power absorbed by the turbine of the cycle [MW]
$W_{FANCondenser}$	Electric power consumed by the air-cooled condenser (hourly average) [MW _{el}]
$W_{HTFPump}$	Electric power consumed by the HTP pump (hourly average) [MW _{el}]
$W_{net,electric}$	Net electric power produced by the solar plant (hourly average) [MW _{el}]
f_{fric}	Friction factor of the flow in the tube
$\eta_{Cycle,Electric}$	Cycle electric efficiency including the electromechanical losses
$\eta_{HTF,elec}$	Electric efficiency of the HTF pump
$\eta_{Optical,Yearly}$	Yearly optical efficiency of the solar field
$\eta_{Thermal,Yearly}$	Yearly thermal efficiency of the receiver
$\eta_{el,mech}$	Electromechanical efficiency of the turbine, the compressor and the pump
$\eta_{sol-El,Yearly}$	Yearly solar to electric efficiency of the CSP plant
ΔP	Pressure drop [bar]
EE	Electric energy yearly [GWh _{el} /year]
$EE_{gross,Yearly}$	Electric energy produced yearly by the power cycle [GWh _{el} /year]
$EE_{net,Yearly}$	Electric energy produced yearly by the CSP plant [GWh _{el} /year]
d	Discount rate
i	Inflation rate
ρ	Density [kg/m ³]

In addition to their higher conversion efficiency, sCO₂ cycles have also been recognized as more cost effective [12]. More efficient flexible transients and satisfactory part load operating conditions have been underlined, additionally, as key differences between sCO₂ cycles and steam cycles, mainly due to the significant reduction in power cycle footprint, a significant higher average density of the working fluid and the widely simplified power block layout with respect to steam cycles (as no bleedings, steam drums, deaerators nor below atmospheric condensation are necessary) [13].

Nevertheless, while CO₂ can be very efficiently exploited as working fluid in air-cooled power cycles with low ambient temperatures (hence low cycle minimum temperatures), the efficiency of sCO₂ cycles sharply drops when the minimum temperature of the power cycles moves to values higher than 40–45 °C, in temperature regions far from the fluid critical point (31 °C): these conditions, in fact, entail higher compressibility factors along the compression step, hence a higher compression work.

Although some studies evidenced the possibility to integrate optimized control practices for CSP plants to work with cooling towers [14], water availability is usually the most relevant issue in typical CSP locations, favoring the adoption of air-cooled condensers for the heat rejection units of the power cycles. At these conditions, the real gas effects during the compression step become less relevant, and pure CO₂ loses some of its interesting characteristics as working fluid for power cycles with respect to steam, compared at the same maximum temperatures.

A possible solution to overcome this limit, proposed within the

SCARABEUS project (EU H2020) [15], is the tuning of the working fluid to match its critical temperature with the ambient temperature, effectively imposing critical temperatures above 70 °C in order to ensure liquid conditions across the whole compression step, which can start above 50 °C and close to the bubble pressure at that temperature. To do so, the research did not point to a different working fluid: on the other hand, binary mixtures of CO₂ and a dopant are considered as innovative working fluids for this application. This way, the beneficial characteristics of sCO₂ cycles over the steam cycles are preserved, and no significant drops in cycle efficiencies are expected for air-cooled solarized cycles at high minimum temperature. This solution can turn supercritical cycles into transcritical ones, as the critical temperature of the suitable dopants is usually much higher than the CO₂ (easily above 150 °C): mixing CO₂ with a dopant that presents a higher critical temperature can in fact increase the critical temperature of the mixture considered as working fluid for the power cycle.

The required characteristics of the selected dopants, in addition to their high critical temperature, are a good thermal stability, limited flammability risks, low toxicity levels, a good overall environmental compatibility and good solubility with CO₂ at the pressures of interest for power cycles. Among them, the most important aspect to consider is the dopant thermal stability: even if CO₂ as pure fluid is considered thermally stable above 700 °C (and therefore it can be adopted in power cycles at this temperature level), the thermal stability of the dopants cannot be taken for granted, effectively imposing a limit on the thermal stability of the overall mixture.

Some previous works literature works identified potential dopants

Table 1
Main characteristics of the pure fluids considered.

CAS	Fluid	T melting [°C]	T boiling [°C]	T critical [°C]	P critical [bar]	Health NFPA 704	Flammability NFPA 704	Reactivity NFPA 704	Thermal stability	Toxicity in air: LC 50/60
115-25-3	C ₄ F ₈	-40	-6	115	27.7	1	0	0	550 °C	LC 60 76,000 ppm/2h
75-05-8	C ₂ H ₃ N	-48	82	270	48.3	2	3	0	550 °C	LC 50 7551 ppm/8h
392-56-3	C ₆ F ₆	4	81	243	32.8	2	1	0	> 600 °C	LC 50 12,488 ppm/2h
124-38-9	CO ₂	-	-78	31	73.8	2	0	0	700 °C	-

for CO₂ based mixtures fluids in the hydrocarbon family, the fluorocarbons, or other non-organic compounds. CO₂ based mixtures with hydrocarbons [16] and refrigerants have been found suitable for low temperature applications [17], around maximum temperatures below 450 °C, easily competing with pure fluid Organic Rankine Cycles (ORC) and outperforming sCO₂ for applications like waste heat recovery from internal combustion engines [18] or biomass plants. Nevertheless, the thermal stability of hydrocarbons is not guaranteed for maximum temperatures of interest for solar tower CSP applications [19]. Other possible solutions for CO₂-based mixtures have been identified in noble gases used as dopants [20], like helium, argon or neon: in those cases, even if the increment in cycle efficiency with respect to sCO₂ cycles has been proved, noble gases cannot move the supercritical conditions of the power cycles into transcritical ones, as the critical temperature of those dopants is lower than the one of CO₂.

Past literature works closer to the framework developed within the SCARABEUS project identified some non-organic compounds as possible CO₂ dopants, such as TiCl₄ or N₂O₄ [21,22]: even if these mixtures clearly lead to an improvement in cycle efficiency with respect to sCO₂ cycles at 700 °C of maximum temperature (assessed with a limited knowledge on the mixture thermodynamic behavior), their high toxicity and significant chemical reactivity makes their handling very difficult from a technical standpoint, since small leakages are normally unavoidable in power plants.

Other works from the SCARABEUS project identified SO₂ as suitable compound [23,24], a dopant that can be of interest for high temperatures applications due to its relevant thermal stability. Even if toxic, it is not reactive nor flammable, and it can be adopted in closed cycles following proper safety procedures and handling of the leaked flows. Assuming a maximum temperature of 700 °C, the recompression power block working with the CO₂ + SO₂ mixture evidenced an absolute increment of 2.1% with respect to the sCO₂ plant (more than 4% in relative terms) assuming a CSP application, always exploiting a higher temperature difference across the storage fluid.

In addition to SO₂, the most investigated dopant in the SCARABEUS project is C₆F₆: both long-term static thermal stability tests and experimental data on the vapor liquid equilibrium (VLE) behavior of the mixture have been taken exclusively for this mixture [25]. The thermal stability results were promising: the CO₂ + C₆F₆ mixture, characterized by a reasonable composition for these applications, has been proven thermally stable for 100 h at 500 °C in a stainless-steel vessel and at 600 °C in Inconel 625. In addition, a preliminary investigation on the performance of this mixture in simple recuperative cycle for CSP applications at 550 °C cycle maximum temperature evidenced the high performance of this solution, presenting almost a 42% cycle efficiency with a cycle minimum temperature above 50 °C [26].

In contrast with previous works dealing with dopants such as TiCl₄, N₂O₄ or SO₂, the three dopants proposed within this work are non-reactive with air, water or metals and their toxicity levels are either limited or negligible: for these key reasons they are investigated and proposed as viable alternative to sCO₂ in power cycles, even if the cycle efficiency increments with respect to them are not comparable to the values obtained with the previously investigated fluids.

2. Selected CO₂ mixtures

While selecting a dopant for an innovative CO₂-based working fluid, the most crucial aspect to consider is the dopant thermal stability, which limits the maximum temperature of the cycle. Given the current state-of-the-art solar tower CSP plants using solar salts as HTF, any selected dopant should be thermally stable at least up to 550 °C, as this value normally represents the turbine inlet temperature of steam Rankine cycles for CSP applications, set by the solar salt thermal stability limit. The second aspect to consider is the fluid reactivity with air or water, crucial during the filling of the power cycle with working fluid, in case of variable inventory configurations and in case of leakages due to failure of a plant component. Then, also the fluid toxicity should be considered, an important characteristic to consider while handling the fluid, even if it can be a less relevant risk in case the fluid is liquid at ambient conditions, and no vapors of the fluid are suspended in air. Nevertheless, other mature technologies, such as ORC, nowadays can employ various flammable organic fluids: at the current technological level, in fact, it is possible to safely handle flammable working fluids in closed cycles, as evidenced in various studies on ORC [27]. Moreover, CO₂ is a fire extinguish agent and it helps reducing the flammability of the overall mixture in case of leakages.

Considering all the reported constraints, three dopants are selected in this work and reported in Table 1, along with some thermodynamic and environmental characteristics and their NFPA rating system. Two of them are fluorocarbons, C₆F₆ (Hexafluorobenzene) and C₄F₈ (Octafluorocyclobutane), a fluid family known for its thermal stability and generally low toxicity levels. The third one, C₂H₃N, is an organic nitrile (Acetonitrile) widely adopted as solvent for the pharmaceutical and chemical industries. The toxicity levels of these inhaled dopants, according to the lethal concentration (LC) limits, are also reported in Table 1: considering that Acetonitrile and Hexafluorobenzene are liquid at ambient conditions, and Octafluorocyclobutane reports very high LC values, in this work it is assumed that all dopants can be adopted in power plants without undermining the life of living beings in the surroundings. The thermal stability limit for C₄F₈ is preliminary fixed at 550 °C in this work, according to the experimental results reported in literature [28], along with the thermal stability of C₂H₃N [29]. On the other hand, the thermal stability of C₆F₆ is assumed at least at 600 °C, as mentioned in the previous chapter [25].

The thermodynamic properties of the investigated CO₂-based mixtures are evaluated using the standard Peng Robinson EoS, with optimized binary interaction parameters (k_{ij}) fitted on the numerous experimental VLE data available for the CO₂ mixture with C₂H₃N ($k_{ij} = 0.054$) [30–33] and the mixture with C₆F₆ [34], as reported in literature [25]. A null binary interaction parameter ($k_{ij} = 0$) is employed for the C₄F₈ mixture due to lack of experimental VLE data: even if this choice limits the robustness of the results for the cycles working with the CO₂ + C₄F₈ mixture, preliminary considerations on this mixture can still be drawn, understanding whether it represents a valid alternative to sCO₂ as working fluid. Afterwards, if the mixture results promising, it will be then possible to perform an experimental campaign on the CO₂ + C₄F₈ mixture to refine the thermodynamic models and the results robustness,

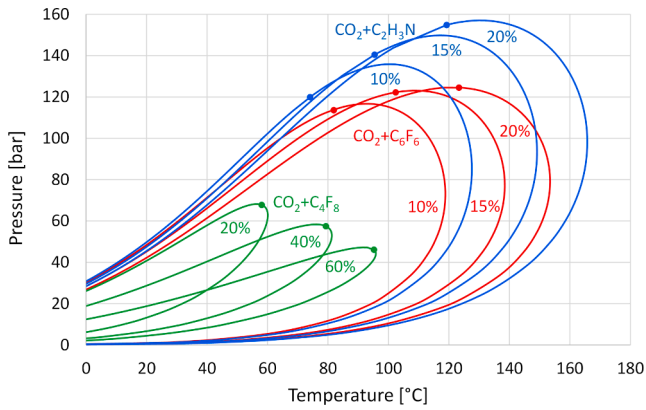


Fig. 1. Pressure-Temperature diagrams for the selected CO₂ mixtures at various dopant molar composition.

as already done with the CO₂ + C₆F₆ mixture [25]. The Span and Wagner EoS is used to model the thermodynamic behavior of pure

carbon dioxide [35]. The pressure–temperature curves for three representative compositions of the mixtures are reported in Fig. 1: as showed, the critical point of the working fluid, evidenced in the figure with a marker, increases its temperature when a higher dopant molar fraction is considered, and it is always higher than the value of pure CO₂ (which is around 31 °C) for any mixture and composition. As a consequence, the three mixtures at any molar composition reported in Fig. 1 can be adopted as working fluid for transcritical cycles condensing at high temperatures (above 50 °C).

Considering the already good performance of the CO₂ + C₆F₆ mixture in transcritical cycles reported in literature within the SCAR-ABEUS project, in this work the pool of CO₂-mixtures investigated for CSP applications is expanded, in order to understand the potentialities of other innovative working fluids and offer a preliminary comparison between their performances.

3. Methodology

This work examines a series of potential next-generation solar tower plants adopting transcritical CO₂-based binary mixtures power cycles.

Table 2

Configurations of cycle maximum temperatures, Storage and HTF characteristics and working fluid studied in this work.

Cycle Maximum Temperature	HTF	Storage Fluid	Storage Configuration	sCO ₂ Cycles	CO ₂ + C ₆ F ₆ Cycles	CO ₂ + C ₄ F ₈ Cycles	CO ₂ + C ₂ H ₃ N Cycles
550 °C	Solar salts	Solar salts	Direct	Considered	Considered	Considered	Considered
550 °C	Sodium	Solar salts	Indirect	Considered	Considered	Considered	Considered
625 °C	Sodium	Innovative salts	Indirect	Considered	Considered	–	–
700 °C	Sodium	Innovative salts	Indirect	Considered	–	–	–

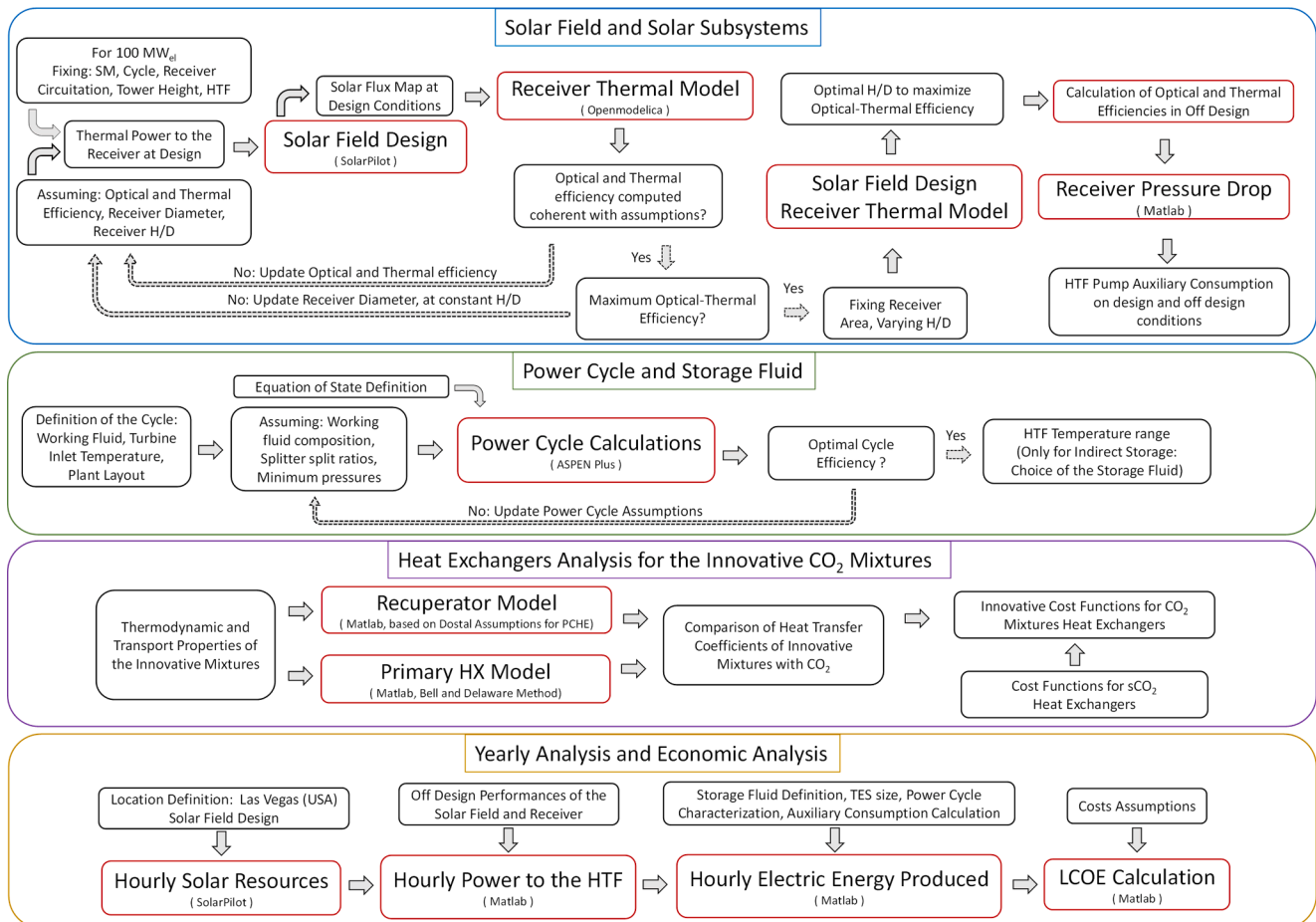


Fig. 2. Block diagram representing the methodology developed in this work.

Three CO₂-based binary mixtures are selected and compared against sCO₂ considering: i) different cycle layouts, ii) different cycle maximum temperatures, iii) direct/indirect storage arrangements and iv) different HTF in the solar receiver. For each plant, the yearly electric energy yield and the LCOE are computed, and the second one is optimized varying the solar multiple (SM) and the TES capacity, assuming Las Vegas (USA) as location. As not all the combinations of working fluids and cycle maximum temperatures are technically feasible, due to the thermal stability limits, the configurations proposed in this work are summarized in Table 2. In addition, Fig. 2 proposes the methodology adopted in this work, along with the main tools adopted.

The next sections will describe the models and the results of this work: in Chapter 4 the solar field design is discussed, the field optical efficiency and receiver thermal efficiency are modelled, along with the electric consumption of the HTF pump of the solar tower, both in design and off design conditions. Chapter 5 proposes the various power block layouts considered and the coupling between the power block and the TES, which is based on the temperature range across the cold tank and the hot tank of the TES. Furthermore, a detailed investigation of the heat transfer characteristics of the innovative CO₂ based mixtures is carried out in Chapter 6: both the primary HX (PHE), as shell-and-tube, and the recuperator, as printed circuit heat exchanger (PCHE), of the power cycles will be designed for each mixture as working fluid. The computed heat transfer area of the two heat exchangers, modelled at constant pressure drop with respect to the sCO₂ configuration, will be used as information to correct the cost of each component adopting CO₂ based mixtures when adopting cost functions for sCO₂ cycles. Chapter 7 lists the cost correlation assumed to model each plant component, from the solar field to the power cycle. Finally, chapter 8 analyses the resulting energy production of each configuration of solar field considered, adopting different working fluids, cycle maximum temperatures, power cycle layouts and storage characteristics. In addition to the technical analysis, all the economic indicators that determine the economic profitability of the CSP plants are reported.

3.1. Key performance indicators

The key performance parameters (KPI) selected for the thermodynamic analysis of the CSP plants are, for each configuration summarized in Table 2: the yearly optical efficiency, the yearly thermal efficiency, the electric cycle efficiency (computed including the electromechanical losses of the compression and expansion steps), the gross yearly electric energy produced, the net yearly electric energy produced, the capacity

inlet and the HTF minimum temperature.

$$\eta_{Thermal,Yearly} = \frac{\sum_{h=1}^{8760} \dot{Q}_{h,HTF}}{\sum_{h=1}^{8760} \dot{Q}_{h,Receiver}} = \frac{\sum_{h=1}^{8760} \dot{Q}_{h,Receiver} \cdot \eta_{h,Thermal}}{\sum_{h=1}^{8760} \dot{Q}_{h,Receiver}} \quad (2)$$

The electric cycle efficiency is computed as reported in Eq. (3), assumed constant as the cycle runs always at full load when thermal power is available. It is computed starting from the mechanical power of the turbomachinery, including their electromechanical efficiencies.

$$\eta_{Cycle,Electric} = \frac{W_{Expansion} \cdot \eta_{el-mech} - \frac{W_{Compression}}{\eta_{el-mech}}}{\dot{Q}_{in,cycle}} \quad (3)$$

The gross yearly electric energy produced by the plant is computed according to Eq. (4) with a simplified control algorithm, considering the hourly thermal energy available both in the storage and in the HTF from the receiver, defocusing part of the heliostats when the thermal input to the cycle is satisfied by the solar plant and the storage is full.

$$EE_{gross,Yearly} = \sum_{h=1}^{8760} \dot{Q}_{h,in,Cycle} \cdot \eta_{Cycle,Electric} \quad (4)$$

In addition, starting from the gross energy produced and the auxiliary consumption of the air-cooled condenser and the HTF circulation pump, the net yearly electric energy is proposed as final thermodynamic KPI, expressed as in Eq. (5):

$$EE_{net,Yearly} = EE_{gross,Yearly} - \sum_{h=1}^{8760} (EE_{h,HTFPump} + EE_{h,AirCondenser}) \quad (5)$$

Finally, as CSP is renowned within the many renewable energy technologies for being dispatchable, the capacity factor (CF) represents a crucial parameter to compare the energy production between various power plants at constant nominal power, computed as in Eq. (6).

$$CF = \frac{EE_{net,Yearly}}{\dot{Q}_{in,cycle} \cdot \eta_{Cycle,Electric} \cdot 8760h} \quad (6)$$

Similarly to the capacity factor, the yearly solar to electric efficiency is the parameter that correlates the yearly electric energy production with the available solar radiation along the year, proposed in Eq. (7):

$$\eta_{sol-El,Yearly} = \frac{EE_{net,Yearly}}{\sum_{h=1}^{8760} DNI_h \cdot A_{SF}} \quad (7)$$

Finally, the main economic performance indicator for the techno-economic analysis of the investigated CSP plant is the Levelized Cost of electricity, computed according to Eq. (8):

$$LCOE \left[\frac{\$}{MWh_{el}} \right] = \frac{CAPEX + \sum_{t=0}^{Lifetime} \left((EE_{net,Yearly} \cdot OPEX_{variab} + OPEX_{fix}) \cdot \frac{(1+i)^t}{(1+d)^t} \right)}{\sum_{t=0}^{Lifetime} \left(\frac{EE_{net,Yearly}}{(1+d)^t} \right)} \quad (8)$$

factor of the power plant and the yearly solar to electric efficiency.

The yearly optical efficiency represents the annual energy collected by the solar field with respect to the annual direct normal irradiation, and it is computed according to Eq. (1): it is expected to increase for smaller solar fields with high solar towers, while it is expected to decrease with receiver of smaller dimensions.

$$\eta_{Optical,Yearly} = \frac{\sum_{h=1}^{8760} \dot{Q}_{h,Receiver}}{\sum_{h=1}^{8760} \dot{Q}_{h,Sun}} = \frac{A_{SF} \cdot \sum_{h=1}^{8760} (DNI_h \cdot \eta_{h,Optical})}{\sum_{h=1}^{8760} DNI_h \cdot A_{SF}} \quad (1)$$

The yearly thermal efficiency is computed considering the instantaneous power hitting the receiver and the power transferred to the HTF, as in Eq. (2). It considers the effects of different receiver dimensions and HTF, along with the influence of the working fluid temperature at PHE

4. Solar field and receiver modelling

In this chapter various solar plants are designed and fully characterized, including both state-of-the-art configurations with direct storage (where the HTF coincides with the storage fluid) and configurations with indirect storage (where the HTF and the storage fluid are two different fluids) for a large-scale solar tower CSP plants, evidencing the most significant implications on the design of the solar components.

As the selection of solar salts in the state-of-the-art CSP cycle as HTF limits the maximum operational temperature of the cycle to the highest allowable temperature of solar salts (assumed at 565 °C), only plants with direct storage and maximum power cycle temperature of 550 °C will adopt solar salts as HTF. For the other solar plants, using sodium as HTF, only the indirect storage configuration is considered, since the

Table 3

Characteristics of the different solar fields designed: geometrical data and optical performances.

Solar Fields Design Assumptions				
Location	Las Vegas			
Geographical Coordinates	N: 36.08° W: 115.17°			
Direct Normal Irradiation at design [W/m ²]	950			
Sun Location at design point	Solar Noon, Summer Solstice Solar Altitude: 77.4°			
Denomination of the Solar Field	Direct 550 °C	Indirect 550 °C	Indirect 625 °C	Indirect 700 °C
HTF temperature range [°C]	421–565	436–580	488–655	540–730
Working fluid maximum temperature [°C]	550	550	625	700
TES Configuration	Direct	Indirect	Indirect	Indirect
HTF	Solar Salts	Sodium	Sodium	Sodium
Storage Fluid	Solar Salts	Solar Salts	Innovative Salts	Innovative Salts
Tower height [m]	195	235	235	235
Heliostat size [m × m]	8 × 10	5 × 7	5 × 7	5 × 7
Heliostat reflectivity/ Fouling factor [-]	0.95/0.95	0.95/0.95	0.95/0.95	0.95/0.95
Surface slope error/ Reflected beam error [mrad]	1.53/0.2	1.53/0.2	1.53/0.2	1.53/0.2
Design Results				
Receiver size				
Height [m]	21.0	15.4	15.1	15.0
Diameter [m]	16.8	14.0	13.7	13.7
Solar field area [m ²]	1,246,240	1,197,315	1,125,950	1,097,460
Number of heliostats	15,578	34,209	32,170	31,356
Nominal optical efficiency [%]	61.78	61.82	62.35	62.82
Maximum solar flux on the receiver [MW _{th} /m ²]	0.972	1.719	1.752	1.719
Overall power on the receiver [MW _{th}]	709.5	682.1	646.9	635.3

solution with direct storage adopting sodium both as HTF and storage media is penalized by a significantly high specific cost per unit of mass and per unit of thermal energy stored [36].

A possible alternative to sodium can be represented by high temperature advanced molten salts: the authors already investigated some advanced molten salts in previous literature works [37,38], underlining the good performances of sodium with respect to these alternatives. In fact, sodium as HTF is widely proposed in literature within the state-of-the-art of high temperature tubular receiver: its main advantage is the high thermal conductivity, that helps limiting the temperature gradient on the tube circumferential direction, therefore limiting the mechanical stresses. Adopting state-of-the-art nickel-based alloys for the receiver tubes, limiting the mechanical stresses is vital to increment the lifetime of the receiver.

In accordance with the HTF selection, different maximum allowable heat fluxes on the receiver must be considered: receivers working with solar salts as HTF are subjected to maximum allowable thermal fluxes of 1 MW/m² [39], while receivers with sodium as HTF can theoretically handle maximum thermal inputs of 2 MW/m² [40]. Therefore, with similar thermal power delivered on the receiver, configurations of receivers with sodium as HTF are expected to have around half the area of the counterpart adopting solar salts, if the design of the receiver is carried out close to the maximum flux condition: hence, due to the lower overall surface, the receiver thermal efficiency can increase even if higher HTF average temperatures are foreseen, counterbalancing the higher convective and radiative losses. Additionally, while the adoption

of sodium as HTF can have positive effects on the thermal efficiency, it also has an impact on the solar field design, since a lower receiver area entails a reduction in optical efficiency at fixed heliostats position.

Considering the various implications regarding the HTF choice and the TES configuration, in this work four different solar towers are designed to be representative of a power plant of around 100MW_{el} in Las Vegas: the first one represents the traditional configuration of state-of-the-art power plants, adopted to achieve cycle maximum temperatures of 550 °C with solar salts as HTF, with a direct storage system. The other three configurations employ sodium as HTF with an indirect storage system: the first for cycle maximum temperatures of 550 °C, the second for 625 °C and the last for 700 °C cycle maximum temperatures. The indirect storage system considered adopts traditional solar salts as storage fluid for the configuration with 550 °C of cycle maximum temperature, and one between NaCl-MgCl₂, NaCl-KCl-MgCl₂ and NaCl-KCl-ZnCl₂ to achieve cycle maximum temperatures above 600 °C, depending on the temperature of the cold tank.

4.1. Solar fields definition and modelling

Four different solar fields are considered in this work, one for each combination of cycle maximum temperature and HTF adopted (presented in Table 2). For each solar field, the design receiver thermal input ($\dot{Q}_{in,rec}$) is obtained through Eq. (9) considering a net power output (P_{net}) of 100 MW_{el}, a SM of 2.4 as in the Crescent Dunes plant [41] and net electric cycle efficiencies ($\eta_{Cycle,Electric}$) of 41%, 44% and 47% for the configuration with cycle maximum temperatures of 550 °C, 625 °C and 700 °C, respectively, according to this work results. The receiver thermal efficiencies (η_{th}) depend on several factors including the HTF thermodynamic properties, the HTF temperature range, the receiver circuitation, and heat flux distribution. For the solar field sizing a first guess values of 85% is considered for the configuration with solar salts, while values of 88%, 86% and 84% are adopted for sodium-cooled receivers with cycle maximum temperatures of 550 °C, 625 °C and 700 °C, respectively. Those value were calculated through the receiver thermal model described in Section 4.2 assuming first-guess receiver characteristics not reported for sake of brevity.

$$\dot{Q}_{in,rec} = \frac{P_{net} \cdot SM}{\eta_{Cycle,Electric} \cdot \eta_{th}} \quad (9)$$

Based on the calculated design receiver thermal input, the solar fields are generated applying the procedure described below and schematically represented in Fig. 2.

Firstly, the case with cycles maximum temperature of 550 °C and solar salt as HTF is treated separately from the other three cases as it represents state-of-the-art molten salts solar towers (except for the HTF minimum temperature which is above 400 °C, instead of the typical value of 290 °C [39]). For this case, the tower height is set to 195 m as for the Crescent Dunes plant, and the receiver dimensions are chosen in order to have a maximum heat flux of 1 MW/m² with an aspect ratio (H/D) of 1.25 [39]. Image Size Priority with a maximum offset factor of two is adopted as heliostats aiming strategy in SolarPilot [42]. The resulting solar field characteristics and receiver dimensions are reported in Table 3.

For the three cases with sodium as HTF smaller heliostats and a higher tower height are assumed to reduce the cosine losses and to compensate for the reduction of the intercept factor and thus of the optical efficiency, caused by the smaller receiver dimensions, which details are provided in Table 3. Both for the solar salts-cooled receiver and the sodium-cooled receiver with a working fluid maximum temperature of 550 °C, the heliostats dimensions (both height and width) were selected optimizing the optical efficiency at design conditions. Afterwards, an iterative optimization procedure is applied to design each of the three solar fields with sodium-cooled receivers and simultaneously determine the corresponding receiver dimensions necessary

Table 4
Assumed characteristics and design performances of the receivers of the solar plants investigated.

Assumptions on the receiver characteristics				
Configuration and HTF	Direct 550 °C, Solar Salts	Indirect 550 °C, Sodium	Indirect 625 °C, Sodium	Indirect 700 °C, Sodium
HTF temperature range [°C]	421–565	436–580	488–655	540–730
Wind speed [m/s]	5.2	5.8	5.8	5.8
Tube material	Haynes 230			
Tube internal diameter [mm]	49.6			
Tube thickness [mm]	1.65			
Tube spacing [mm]	2			
Tube absorptivity [%]	94			
Tube emissivity [%]	87			
Number of panels per flow path	7	4	4	4
Number of flow paths	2	2	2	2
Resulting characteristics of the receiver and design performances				
Number of tubes per panel [-]	68	100	98	98
Overall number of tubes [-]	952	800	784	784
Thermal efficiency [%]	85.9	88.4	87.1	85.8
Specific thermal losses [kW _{th} /m ² _{receiver}]	90.2	116.8	128.5	139.7
Thermal power to the HTF [MW _{th}]	609.5	603.0	563.4	545.1
HTF mass flow rate [kg/s]	2768	3313	2687	2292

to deliver the receiver thermal input, as proposed in Eq. (9). In detail, for the three plants with sodium as HTF, the receiver diameter and height are varied (with a 0.1 m step in diameter) fixing the H/D aspect ratio to 1.25 (similarly to Crescent Dunes), while the solar field is generated in SolarPilot. After this first iteration loop, the receiver area was fixed, according to the condition with maximum optical-thermal efficiency in design conditions. Finally, a second iteration loop is added, fixing the receiver area and varying the receiver aspect ratio to find its optimal value according to the same criterion. The thermal efficiencies are calculated with the aid of the receiver thermal model presented in Section 4.2. Also in this case, Image Size Priority with a maximum offset factor of two is adopted as heliostats aiming strategy [42]. Results of all the investigated configurations for each of the three solar fields are not reported for sake of brevity, but the characteristics of the optimal solar field and receiver obtained for each case are reported in Table 3. The latter shows how, when sodium is adopted HTF, the optimal receiver aspect ratio computed according to this procedure is 1.1, while the optimal peak heat flux results about 1.7 MW/m² for all the cases, thus below the value 2 MW/m² considered as typical limit for sodium-cooled receivers [43]. This is consistent with the results obtained by Asselineau [44], who showed that the optimal maximum flux for sodium receivers is not necessarily 2 MW/m², as this condition significantly penalizes the optical efficiency.

As a result, the difference in optical efficiency between the various solar plants is limited: sodium-cooled receivers benefit from an increment in tower height with respect to the solar salts-cooled receiver, the cosine effects are reduced, counterbalancing the spillage losses. Moreover, the progressive reduction in the overall thermal power to the receiver for the sodium-cooled receivers and the subsequent reduction in solar field dimension also entails an increment in optical efficiency.

Once the four solar fields are generated, SolarPilot is adopted to obtain the optical efficiency of each heliostats field as function of the solar azimuth and zenith. Such optical efficiency maps will be then adopted for the plant yearly analysis described in Chapter 8 on an hourly discretization basis.

4.2. Receivers definition and modelling

For the four different receivers investigated in this work (reported in Table 3), the number of panels for each flow path of the receiver was taken from literature: for the receiver with solar salts as HTF the characteristics of crescent dunes receiver are adopted, while for the receivers with sodium a reference condition from literature was assumed [37]. The tubes diameter and thickness are assumed between the standard pipes sizes [45] and the number of tubes per panels are computed ensuring a spacing between the tubes of 2 mm [46]. The main receiver characteristics and operating conditions are reported in Table 4. The HTF temperature range is selected considering a 15 °C temperature difference at the cold- and hot-ends of both the HTF-to-storage fluid HX and of the power cycle PHE, assuming the power cycle working with the CO₂ + C₆F₆ mixture in simple recuperative configuration as reference case for the innovative technology adopting CO₂-based cycles.

The design and off-design thermal efficiencies of the four receivers are obtained through the Modelica package SolarReceiver2D [47] that enables two-dimensional dynamic thermal simulation of external cylindrical receivers working with any type of HTF and temperature range. The model discretizes the tubes in finite volumes (along the axial and circumferential direction), computing the reflective losses (assuming the tube emissivity reported in Table 4), the convective losses and the radiative losses on each finite volume. The radiative losses are modelled accounting for view factors from each of the finite-volume of the receiver tubes toward the external environment, computed according to the crossed strings method. Additional details on the thermal model and the receiver circuitation can be found in Appendix A. The wind speed on the tower is assumed as function of the receiver altitude as a yearly average value for the location [48]. In detail, only the design heat flux map is generated in SolarPilot and then proportionally scaled from 20% to 100% with an increment of 10%. The resulting heat flux maps (nine for each of the four solar fields) are given as input to the receiver thermal model to estimate the thermal efficiency as function of the ratio between receiver thermal input and design thermal input. This approach is based on the assumption that the thermal efficiency depends only on the overall power input while is barely affected by the heat flux distribution [11]. In addition, the receiver thermal efficiencies are evaluated for different values of design working fluid temperature at the inlet of the PHE, assuming a cold end temperature difference of 15 °C both between the HTF and the storage media and between the storage media and working fluid. The resulting thermal efficiency maps, which will be adopted for the plant yearly analysis described in Chapter 8, are reported in Fig. 3. The latter shows how the thermal efficiency strongly depends on the working fluid temperature at the inlet of the PHE when sodium is adopted as HTF. Moreover, the use of sodium is beneficial to the thermal efficiency for all configurations, when compared to solar salts, even at much higher temperatures, due to the significant reduction in receiver area. Accordingly, the indirect configuration with sodium as HTF and salts as storage fluid (Fig. 3(b), (c), (d)) presents evident advantages in terms of thermal efficiency with respect to the direct TES configuration (Fig. 3(a)).

4.3. Modelling of HTF pumping system

The HTF pump allows the HTF circulation from ground level up to the top of the solar tower, where the receiver is installed. For direct storage systems, the geodetic head provided by the pump is dissipated when the HTF enters the hot tank. In case of indirect storage systems, instead, the HTF flows in a closed loop between the receiver and the

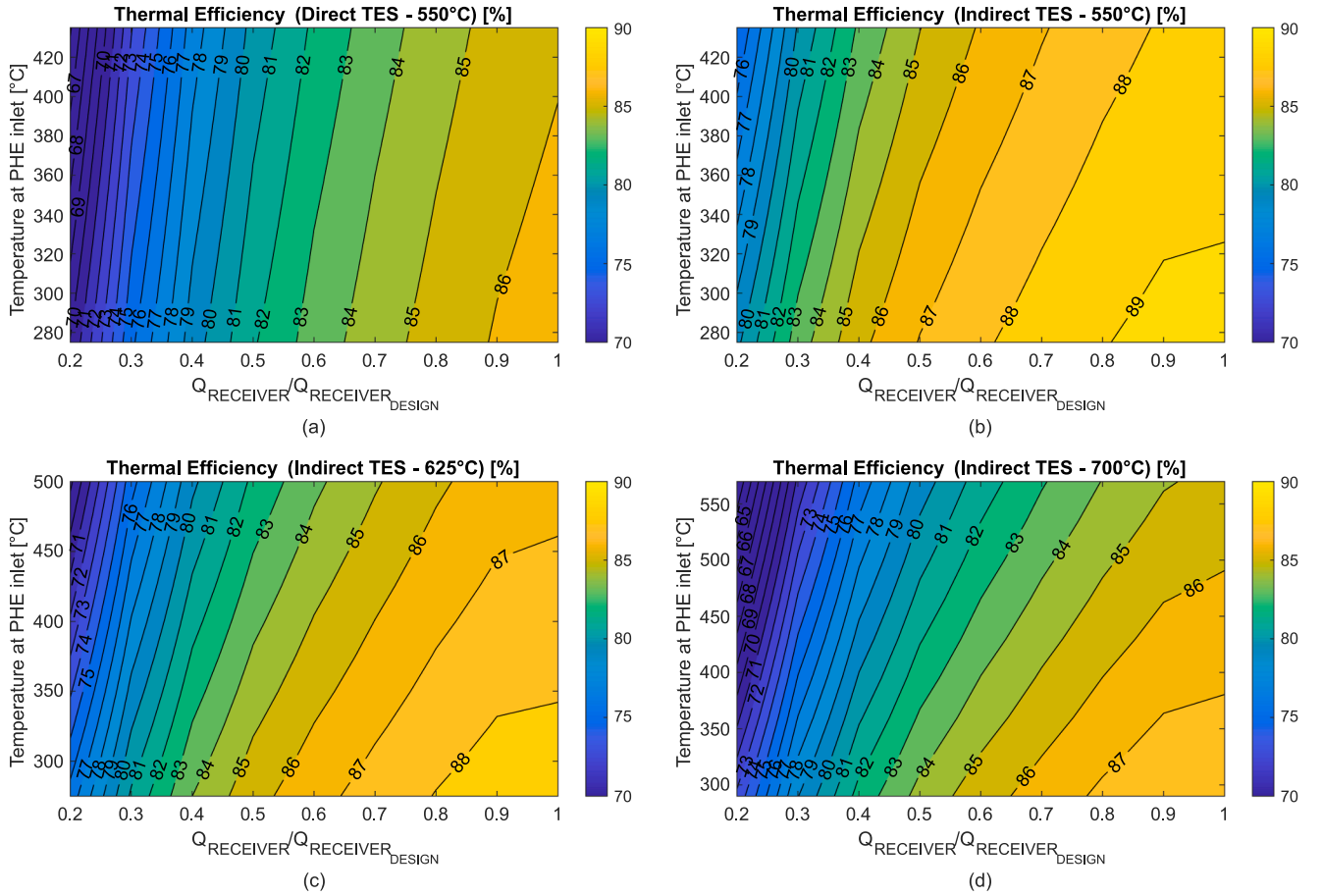


Fig. 3. Thermal efficiency maps for the four receivers considered in this work: direct 550 °C (a), indirect 550 °C (b), indirect 625 °C (c), indirect 700 °C (d). The denomination of the receivers refers to the ones proposed in Table 3.

HTF-to-storage-fluid heat exchanger, where the HTF is cooled down: in this case the HTF pump head is only attributed to the compensation of the concentrated and distributed friction losses in the receiver, since the distributed pressure drops in the piping and the pressure drops in the PHE or in the HTF to storage heat exchanger are neglected for all configurations. In literature shell and tubes HXs are proposed for the HTF-to-storage fluid HXs: given the very high temperatures involved, costly materials must be adopted. Nevertheless, given the high densities of the two fluids and their performant heat transfer characteristics, relatively low areas per unit of heat transfer can be assumed. Other types of HXs, such as printed circuit heat exchangers, may lead to risks of clogging on the molten salts side due to unforeseen adverse local temperature gradients. For this reason, molten salts are proposed in the shell-side of the HX, free to move along the baffle-to-shell clearances in case any clog occurs. No specific analyses are proposed for these HX in this paper, while an in-depth analysis of the working fluid-to-storage fluid PHE is carried out in chapter 6, as the investigation of the different innovative working fluid characteristics is the main focus of this work.

Focusing on the pressure drop in the receiver tubes, the model adopts the receiver circulations reported in Table 4, where each panel is connected to the subsequent one through a collector. A constraint on the maximum HTF velocity in the tubes of 4 m/s has been verified, ensuring to avoid erosion problems. The pressure drop of the HTF, across each tower-receiver system, are computed according to Eq. (10), as the sum of the geodetical term (considered only in case of direct storage) and of the receiver concentrated and distributed pressure losses, in accordance with the receiver model adopted [42].

$$\Delta P_{tot} = (\rho_{HTF} \cdot g \cdot h_{Tower})_{direct} + N_{panels} \cdot \left(\frac{f_{fric} \cdot L_{tube}}{2 \cdot D_{in,Tube}} \cdot \rho_{HTF} \cdot V_{HTF}^2 + \sum_i K_i \cdot \rho_{HTF} \cdot \frac{V_{HTF}^2}{2} \right) \quad (10)$$

In the adopted hydraulic model, the concentrated pressure drop coefficient K_i is dependent on the receiver circutation and the types of concentrated pressure losses underwent by the HTF. In this work, a K_i of 0.6 and 0.5 at manifold inlet and outlet is considered, along with a K_i of 0.13 for each 90 °C bend, and other K_i values modelled according to literature [49] accounting for the various T joints from the tubes to the manifold and from the manifolds to the tubes.

Finally, assuming a constant HTF electric pump efficiency $\eta_{HTF,elec}$ of 80%, the auxiliary electric consumption of the circulation pump is computed as in Eq. (11), for each HTF mass flow rate \dot{m}_{HTF} , representing different values of thermal power absorbed by the HTF.

$$W_{HTFPump} = \frac{\dot{m}_{HTF} \cdot \Delta P_{tot}}{\rho_{HTF} \cdot \eta_{HTF,elec}} \quad (11)$$

The maps reported in Fig. 4 quantify the electric power (in MW_{el}) consumed by the HTF pump as function of the thermal power to the receiver and the temperature of the working fluid at the inlet of the PHE at design conditions (univocally determined for each power cycle – solar plant combination). The computed HTF pump consumption in the direct storage configurations is significantly higher than the indirect configurations (due to the influence of the geodetical term), with the highest relative difference in off design conditions where the power incident on the receiver is lower than the design value due to a reduction in HTF mass flow rate.

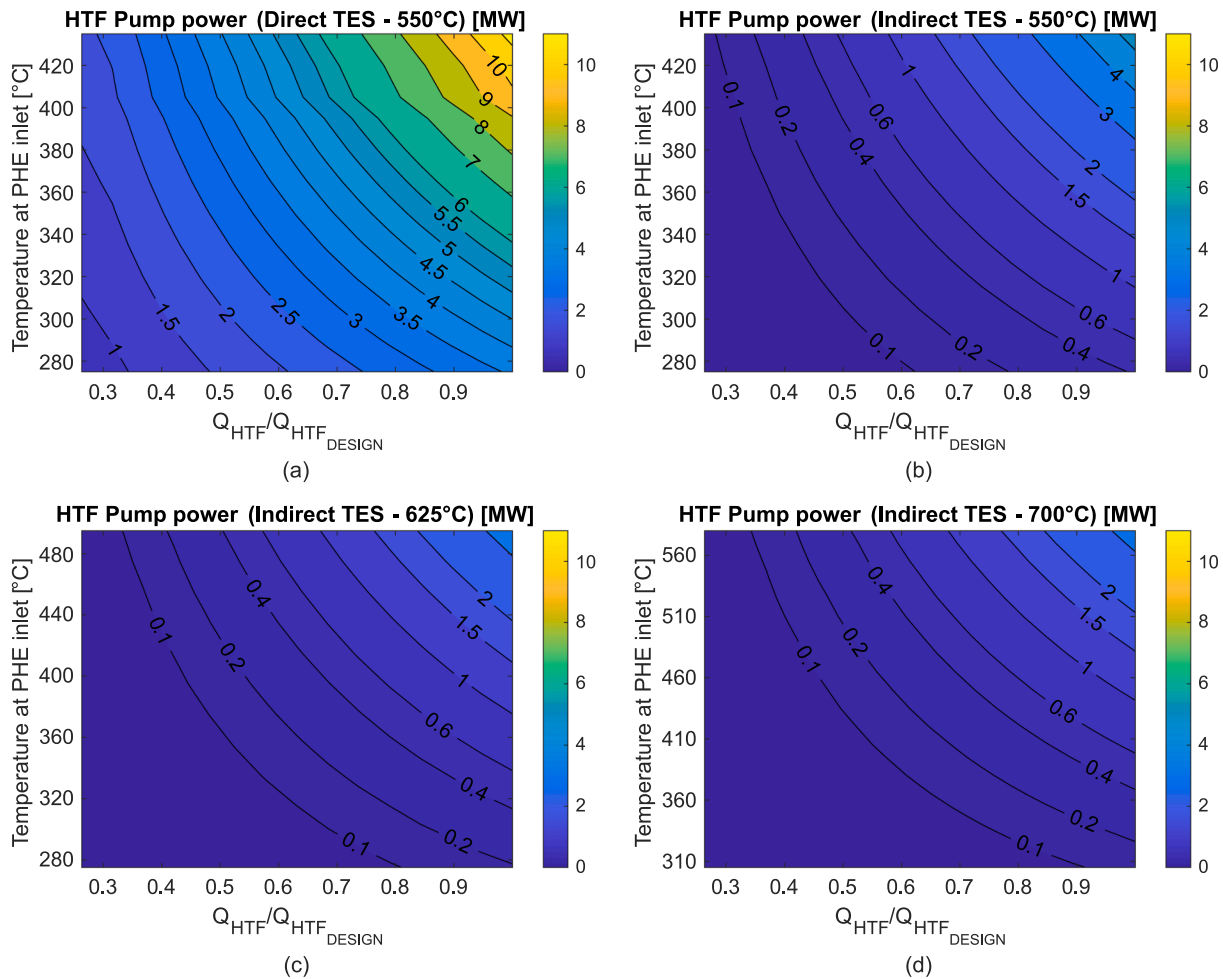


Fig. 4. HTF pump auxiliary consumption maps for the four solar fields considered in this work, expressed in MW_{el} : direct 550 °C (a), indirect 550 °C (b), indirect 625 °C (c), indirect 700 °C (d). The denomination of the four solar plants refers to the ones proposed in Table 3.

According to the results presented in terms of solar field optical efficiency and receiver thermal efficiency, the considerations on the solar field area and accounting for the drastic reduction of the auxiliary consumption of the HTF circulation pump, the indirect storage configuration appears more promising than the direct one for any HTF temperature range across the receiver.

From an energetic point of view, the drop in optical efficiency for the configurations with indirect storage and sodium as HTF, with respect to direct storage plants with solar salts, can be balanced increasing the solar tower height, and the thermal efficiency computed can increase by 2.5% at constant HTF temperature range, so that indirect storage solutions with cycle maximum temperatures around 700 °C presents comparable thermal efficiencies to direct storage solutions with cycle maximum temperatures of 550 °C. Finally, the HTF pump consumption can be reduced by a factor from 5 to 10, depending on the thermal input to the receiver. As a matter of fact, the HTF pump auxiliary consumption for a direct storage system based on solar salts in Fig. 4(a) is considerably high for any value of working fluid temperature at PHE inlet. In this particular case, with a reference plant of around $100MW_{el}$, the HTF pump consumes up to $10MW_{el}$ at design conditions, for a recompressed sCO_2 cycle with high PHE inlet temperature. Even if this peak electric consumption is experienced for a minor fraction of operating hours, due to the effects of high solar multiple and DNI lower than the design value, the adoption of an indirect storage is a determining factor in cutting this significant source of parasitic electric consumption.

5. Power cycle and thermal energy storage coupling

5.1. Selection of power block layouts

In recent years, sCO_2 cycles have been studied for various applications evidencing different optimal cycle layouts for each application. For example, when waste heat recovery is explored, the simple recuperative layout with bypass or the cascade layout have been identified as optimal configurations [50], while the recompression layout is usually proposed as highly performant for CSP applications, mainly due to the high cycle efficiency [51]. Nevertheless, this solution comes at the cost of a very poor heat recovery from the hot source, entailing a working fluid temperature difference across the PHE between 100 °C and 150 °C, with a significant auxiliary consumption of the HTF pump.

On the other hand, considering transcritical cycles working with CO_2 -based mixtures, as a recent work describing the thermodynamic behavior of the $CO_2 + SO_2$ mixture evidenced, a substantial increment in heat recovery capacity from the hot source can be evidenced, both for highly efficient layouts (as the recompression) and for layouts devoted to heat recovery applications [23].

As a matter of fact, the adoption of CO_2 -based mixtures for transcritical cycles in CSP applications helps shifting the paradigm typical of sCO_2 cycles that easily identifies the recompression layout as the most promising one: in this work, instead, starting from the simple recuperative cycle, also the cascade and the precompression layouts, shown in Fig. 5, are included. These two layouts, able to recover heat from the HTF across a wider temperature difference, are considered as promising

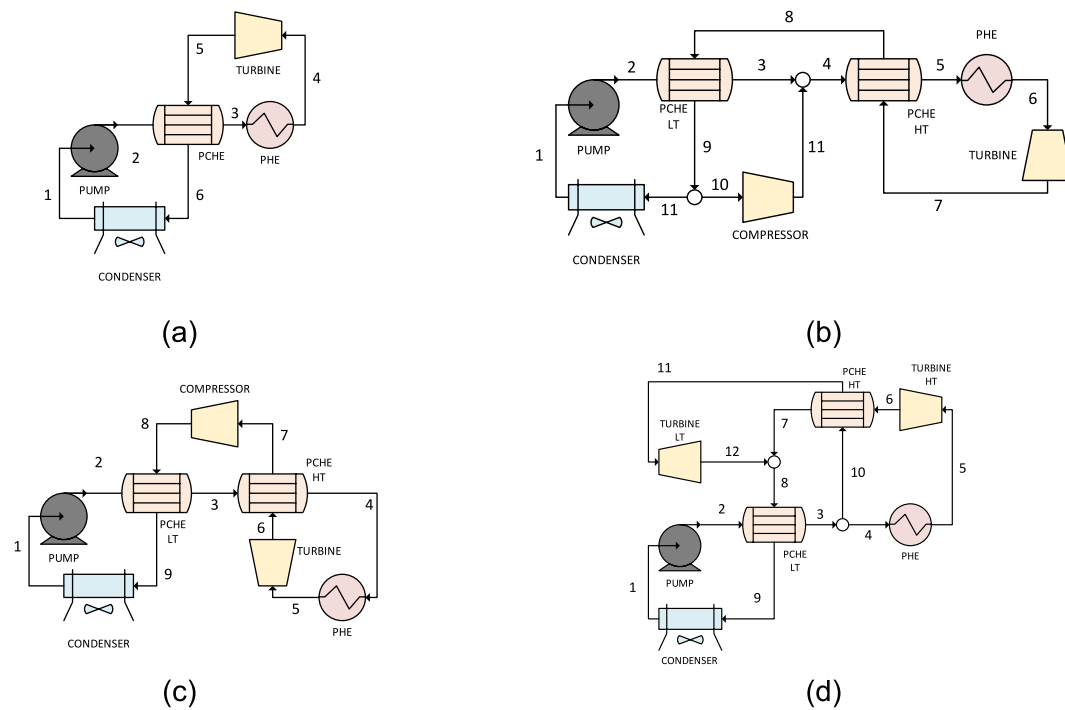


Fig. 5. Power block layouts adopted in this work for CSP applications: Simple recuperative (a), Recompression (b), Precompression (c) and Cascade (d).

Table 5
Main assumptions for the power cycle analyses [25].

Parameter	Value
Turbine inlet temperature [°C]	550–625–700
Turbine isentropic efficiency [%]	92
Pump inlet temperature [°C]	51
Compressor/Pump isentropic efficiency [%]	88
Motor/Generator electro-mechanical efficiency [%]	99
Recuperator Minimum Internal ΔT [°C]	5
Recuperator Pressure drop HP [bar]	0.5
Recuperator Pressure drop LP [bar]	1
Primary HX Pressure drop [bar]	4
Condenser Pressure drop [bar]	2
Turbine inlet pressure [bar]	253
Air-cooled condenser design fan consumption [% of Q_{cond}]	0.85
Design ambient temperature [°C]	36

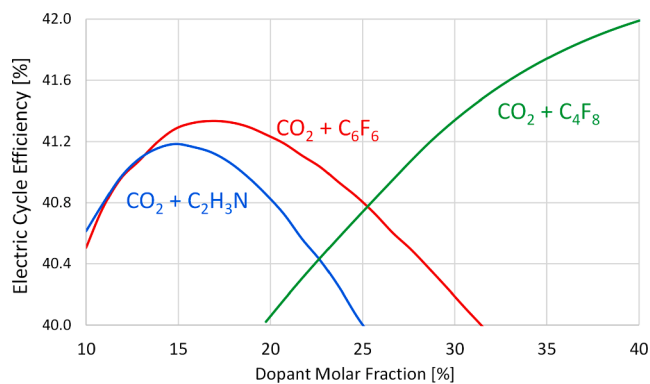


Fig. 6. Results of the analysis of the optimal dopant fraction on the electric cycle efficiency in the three selected mixtures for the simple recuperative cycle layout with a maximum temperature of 550 °C.

candidates for the application in CSP plants, along with the recompression layout. The precompression layout can help increasing the

cycle efficiency and the specific work, with respect to the simple recuperative layout, by expanding the flow in the turbine to a lower pressure, introducing a pressure difference that is compensated in a secondary compressor after the high temperature recuperator. On the other hand, the cascade layout has the characteristic to exploit a single compression step across the whole power block and it allows tuning the PHE inlet temperature by properly modifying the split ratio after the first recuperator.

All the cycles are modelled in ASPEN Plus v.11 [52] and the main assumptions adopted are reported in Table 5.

For each combination of mixture, cycle layout and cycle maximum temperature, a sensitivity analysis on the mixture molar fraction is performed, with the goal of maximizing the cycle efficiency defined as in Eq. (3).

For representation purposes, the trends of the simple recuperative cycle efficiencies as function of dopant fraction for each mixture are plotted in Fig. 6, assuming a cycle maximum temperature of 550 °C: while for C_2H_3N and C_6F_6 a clear optimum composition is found in the 10–20% dopant molar fraction range, mainly related to the position of the critical temperature (optimal in the range between 80 °C and 90 °C), these values of critical temperatures are not obtainable with a limited amount of C_4F_8 in the mixture, as presented in Fig. 1. In fact, imposing around 30 °C to 40 °C of temperature difference between the cycle minimum temperature and the critical point of the mixture allows to have the best trade-off between the reduction in compression work (pumping the flow in the liquid phase) and maintaining a relatively high cycle pressure ratio, necessary to maximize the cycle efficiency. For this reason, the composition of the C_4F_8 mixture was not chosen to maximize the cycle efficiency but to have a cycle efficiency in the same range of the other two mixtures, limiting the molar fraction of C_4F_8 to 27%, corresponding to a 63% mass fraction, in order to still have a non-negligible presence of CO_2 in the mixture.

For the precompressed layout the turbine outlet pressure is included as additional optimization variable, while, for the cascade layout, the splitter mass ratio (i.e. m_{10}/m_3 in Fig. 5(d)) is set in order to have both the cold and hot end temperature difference in the HT recuperator equal to the minimum allowed internal temperature difference (i.e. 5 °C).

Table 6

Optimal mixture composition, cycle electric efficiency and temperature at PHE inlet for the analyzed mixtures and for pure sCO₂ as function of the plant layout, at cycle maximum temperatures of 550 °C.

		Simple Recuperative	Precompressed	Recompressed	Cascade
Dopant molar fraction [%]	CO ₂ + C ₆ F ₆	16	15	–	16
	CO ₂ + C ₄ F ₈	27	27	27	27
	CO ₂ + C ₂ H ₃ N	15	13	–	15
Cycle Electric Efficiency [%]	CO ₂ + C ₆ F ₆	41.3	42.2	–	39.2
	CO ₂ + C ₄ F ₈	40.9	42.0	43.4	38.8
	CO ₂ + C ₂ H ₃ N	41.2	41.9	–	39.2
	Pure CO ₂	37.4	40.0	41.7	35.5
Working fluid Temperature at PHE inlet [°C]	CO ₂ + C ₆ F ₆	406	400	–	293
	CO ₂ + C ₄ F ₈	408	405	425	296
	CO ₂ + C ₂ H ₃ N	364	361	–	293
	Pure CO ₂	384	409	418	293

Table 7

Characteristics of the four storage fluids considered in this work [38].

Storage Fluid	Composition [% mol]	Melting Point [°C]	Maximum Temperature [°C]	Cost [\$/kg]
NaNO ₃ + KNO ₃ (Solar Salts)	64% + 36%	223	601	0.80
NaCl + MgCl ₂	58% + 42%	445	1465	0.12
NaCl + KCl + MgCl ₂	30% + 20% + 50%	397	Above 700 °C	0.23
NaCl + KCl + ZnCl ₂	13.8% + 41.9% + 44.3%	229	Above 700 °C	0.69

The optimized dopant fractions for each cycle layout and mixture, together with the temperature at the inlet of the primary heat exchanger, are presented in Table 6 with the electric cycle efficiency. The investigation of the optimal molar fraction of the CO₂ + C₆F₆ mixture for the power cycles with maximum temperatures of 625 °C, not reported in Table 6, presented the same results of the reported conditions with 550 °C of cycle maximum temperature.

For C₆F₆ and for C₂H₃N the recompressed layout is not considered, since it is not possible to reach single-phase conditions at the inlet of the compressor (point #10 in Fig. 5(b)) in the simulations, due to the extended range of the VLE region for any composition, as shown in Fig. 1. On the other hand, for the CO₂ + C₄F₈, as already reported for the simple cycle, the optimal molar composition is limited to a maximum

value of 27% for C₄F₈ in all the cycle architectures.

A second relevant cycle parameter is the working fluid temperature at the PHE inlet. This parameter strongly influences the achievable cycle efficiency, the receiver thermal efficiency and the cost of the storage section, as the higher the temperature difference of the storage fluid across the PHE, the lower the HTF mass flow rate in the receiver, with small TES volume and lower costs at constant thermal input. Under this perspective, the CO₂ mixture with C₂H₃N is significantly more performant than the other working fluids.

The net plant electric power is finally computed from turbomachinery gross mechanical power considering generators and motors electro-mechanical losses and air-cooled condenser and HTF pump consumption:

$$W_{net,electric} = \eta_{Cycle,Electric} \cdot \dot{Q}_{in,cycle} - W_{HTFPump} - W_{FANCondenser} \quad (12)$$

The air-cooled condenser fan consumption is assumed equal to 0.85% of the heat rejected at the condenser at design conditions, when the ambient temperature is 36 °C, while the HTF circulation pump consumption was already discussed in Eq. (11) and it is reported in Fig. 4.

During the year, the power block is always operated at full-load, when thermal power is available, and with constant cycle minimum temperature, considering as the only off-design effect the impact of the ambient temperature on the air condenser fan rotational speed [53]. The fan consumption is computed as function of the mass flow rate of the air, as already proposed in literature, for any ambient temperature [54]: the simplified approach can help in comparing performances of different power cycles independently from their off-design performances. Nevertheless, future works developed within the SCARABEUS project

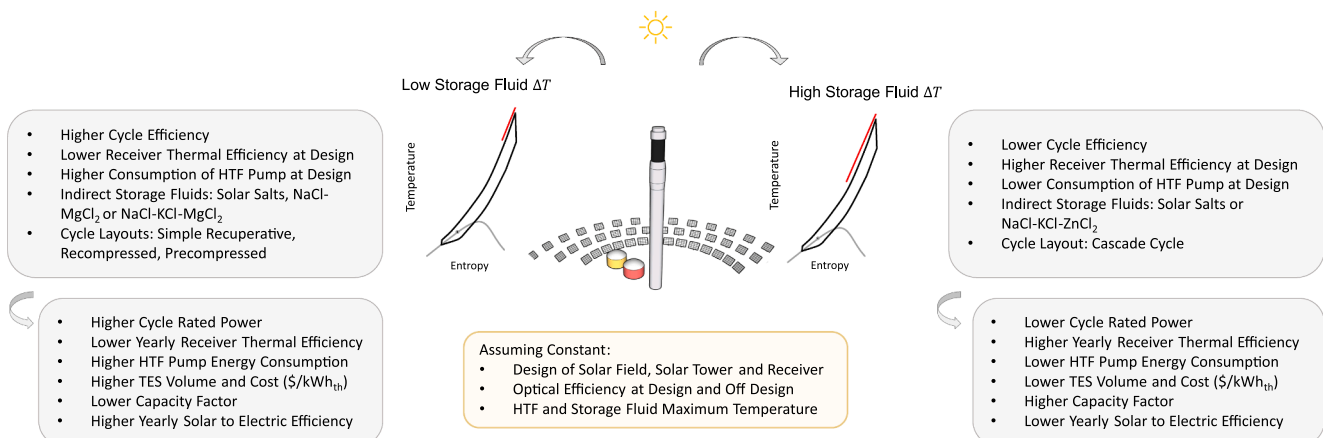


Fig. 7. Differences between a high heat recovery and a low heat recovery power cycle for CSP configurations working with CO₂-based fluid.

Table 8
Characteristics of the PCHE modelled for sCO₂ and CO₂-based mixtures cycles.

Parameter	Value
Channel diameter [mm]	2
Plate thickness [mm]	0.5
Pitch between channels [mm]	2.4
Internal surface roughness [mm]	0.01
Material	Stainless Steel 316
Material Thermal conductivity [W/m/K]	15

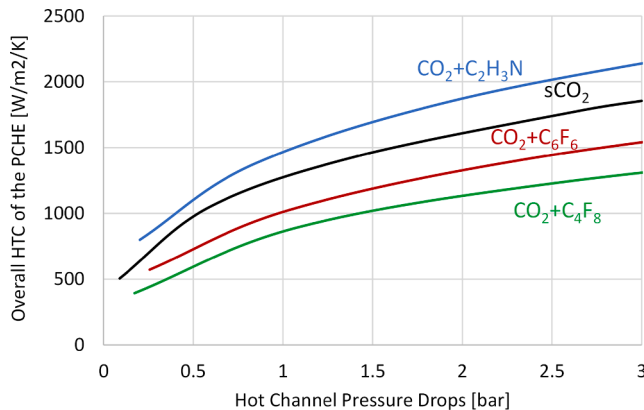


Fig. 8. Dependency of the recuperator (PCHE) overall HTC on the pressure drop in the hot channel for the simple recuperative cycles working with different CO₂ mixtures and sCO₂.

will investigate the off-design conditions of the proposed transcritical cycles.

5.2. Storage media selection, cycle and solar field match

Four different storage fluids are considered in this work, selected as the least expensive among a large pool presented in a previous work detailing different HTF and storage fluids for CSP [38]. For all the configurations characterized by a power cycle maximum temperature of 550 °C, state-of-the-art solar salts are selected, both for the direct and indirect storage configurations. In the two solar fields designed for cycle maximum temperatures of 625 °C and 700 °C, the optimal storage fluid is selected according to the cold tank temperature, fixed 15 °C above the working fluid temperature at the inlet of the PHE.

NaCl + MgCl₂ is adopted as storage fluid for cold tank temperatures higher than 460 °C; below this temperature it cannot be used due to the proximity to the fluid melting point. For cold tank temperatures between 415 °C and 460 °C NaCl + KCl + MgCl₂ is adopted as storage fluid, while for lower cold tank temperatures (i.e. below 415 °C) the fluid selected is NaCl + KCl + ZnCl₂. All the considered storage fluids are listed in Table 7, along with their composition and costs, where the more costly are the ones with a low melting temperature. On one hand, increasing the temperature difference between the hot and cold tank has a beneficial impact on the storage fluid inventory, on the HTF pump auxiliary consumption (see Fig. 4) and on the receiver thermal efficiency (see Fig. 3), while, on the other hand this has a negative impact on the fluid specific costs in mass terms. Under this perspective, it is important to remember that the storage cost accounts for a fraction between 15% and 30% of the overall CSP plant cost [55], mainly depending on the storage capacity.

Since both the receiver thermal efficiency and the TES dimension are affected by the coupling between the solar plant and the power block layout, the optimal techno-economic configuration will inevitably be influenced by these factors, as lower TES specific costs and lower cycle efficiencies are two contrasting effects. In Fig. 7 it is qualitatively summarized the impact of the temperature difference across the PHE and

consequently the one between the hot and cold storage tanks on system performance and cost.

6. Impact of the use of CO₂ mixtures on heat exchanger design and costs

The heat transfer characteristics of the selected CO₂ mixtures and their impact on the power cycles heat exchangers design and cost will be analyzed in this chapter. In particular, detailed models for a shell-and-tube (S&T) PHE and the PCHE recuperators are developed for these comparisons. As a previous study comparing condensers for CO₂-based mixtures and heat rejection units for sCO₂ cycles concluded that the variation in heat transfer coefficients is not particularly significant [56], only the PHE and the recuperator will be analyzed in this work.

Cost correlations for the capital costs of sCO₂ heat exchangers are usually related to the product between the heat transfer area (*A*) and the overall heat transfer coefficient (*U*) [8,57]. This is a simplification, since two fundamental aspects are generally not considered: i) the dependence of the *UA* size parameter on the pressure drops of both sides of the HX, ii) the dependence of the *UA* size parameter on the actual heat exchanger material, that strongly influences the design and the costs. Regarding the HX material, a few cost functions include a temperature-dependent parameter (as the ones reported in Weiland for the recuperator) that can help to properly estimate the impact of the material on the cost, as different temperature levels entail different materials: nevertheless, this dependency is not commonly included in cost functions of all the heat exchangers. Finally, as the cost correlations are developed for sCO₂ and heat exchangers of sCO₂ cycles, they are not directly applicable to CO₂ mixtures as working fluids, since different working fluids exchange heat differently, if employed in the same heat exchanger, as both their thermodynamic and transport properties are different.

In the following analyses on the PCHE and on the S&T, the materials will be fixed: Inconel 617 will be adopted for the S&T and Stainless Steel 316 in the PCHE. Inconel 617 is expected to have good material compatibility with high temperature working fluids, but also to have higher costs. Stainless steel is a cheaper material already adopted for low temperature (i.e. below 550 °C) heat exchangers [58], nonetheless it can still be representative of a power cycle operating at high temperatures.

The effect of the working fluids pressure drops on the heat exchangers design are included in this work: higher pressure losses generally entail higher velocities of the fluids and therefore higher heat transfer coefficients with lower CAPEX, while compromising the cycle efficiency. For this reason, the heat transfer performances of the two main heat exchangers will be examined in a wide range of pressure drop on the power cycle side. Appendix B reports the models adopted for the calculation of the transport properties, the heat transfer coefficients and the friction factors of both CO₂ and CO₂ mixtures. On the basis of the specified assumptions, the following two chapters will propose a comparative PCHE and S&T design for the four selected working fluids. The study is performed specifically on the simple recuperative cycle layout with a maximum temperature of 550 °C, but the obtained results will be extended also to the other cycles layouts.

6.1. Printed circuit heat exchangers recuperators

In this work four PCHE recuperators (one for the sCO₂ cycle and three for the cycles working with the three mixtures) are designed in MATLAB considering standard straight semicircular channels. In accordance with the work of Dostal [59], a single pair of channels is modelled and considered representative of all the channels in the PCHE. The geometric assumptions on the PCHE and on the material are reported in Table 8, and the modeling of the PCHE for sCO₂ and CO₂ based mixtures recuperators is detailed in Appendix C.

The design temperature and pressure ranges on the two sides of the recuperators for the four cases are listed in Appendix E, resulting in

Table 9

Fluid correction factors adopted to correct the literature costs function of the PCHE, on the basis of the PCHE cost for CO₂.

	CO ₂ + C ₆ F ₆	CO ₂ + C ₂ H ₃ N	CO ₂ + C ₄ F ₈
CO ₂ Molar fraction	84%	85%	73%
HTC variation compared to pure CO ₂ (at constant ΔP)	-18%	+17%	-30%
Fluid Correction Factor for PCHE cost, $f_{U,PCHE,Mix}$	1.16	0.89	1.31

similar temperature ranges, same high pressure and different low pressures. While the low-pressure side of the sCO₂ cycle is optimized to maximize cycle efficiency, the low-pressure level of the transcritical cycles working with CO₂ mixtures is set by the bubble conditions of each mixture at the cycle minimum temperature. The resulting PCHEs have been designed in a wide frictional pressure drop range on the hot-side channel (modifying the mass flow rate flowing in the single channel).

The trends of the overall heat transfer coefficients as function of the pressure drop for the different CO₂ mixtures are reported in Fig. 8: results show a reduction of about 18% and 30% of the overall heat transfer coefficient with respect to pure CO₂ for the CO₂ + C₆F₆ and the CO₂ + C₄F₈, respectively. Inversely, the adoption of the CO₂ + C₂H₃N mixture shows improved heat transfer performance, by around 17%. The results underline that the effects of adding a dopant to a pure fluid can strongly influence the heat transfer characteristics of the mixture, and thus the implications on the heat transfer area and the heat exchanger cost are not negligible. If the same mean log temperature difference between the two sides of the recuperator and the same heat exchange are assumed, the increase/reduction in the overall heat transfer coefficient corresponds to the same reduction/increase in heat transfer area.

According to the cost correlations in literature for PCHE suitable for sCO₂ cycles [58], the heat exchanger cost is proportional to UA, with a scale factor of 0.7544, as reported in Eq. (13):

$$C_{PCHE,CO_2} = a \cdot (UA)^{0.7544} \cdot f_T \quad (13)$$

Assuming that the cost of a heat exchanger is strictly related to its heat exchange area (and therefore its volume), the cost of the recuperator for a CO₂ mixture can be evaluated from the pure CO₂ case adopting the same scaling equation, with a correction factor $f_{U,PCHE,Mix}$, reported in Eq. (14).

$$f_{U,PCHE,Mix} = \left(\frac{U_{CO_2}}{U_{Mix}} \right)^{0.7544} \quad (14)$$

The obtained fluid correction factors computed according to the results of Fig. 8 for the PCHE costs are reported in Table 9. The cost function for PCHEs adopted in this work will thus have the following form:

$$C_{PCHE,Mix} = f_{U,PCHE,Mix} \cdot C_{PCHE,CO_2} \quad (15)$$

6.2. Shell and tubes primary heat exchanger

In addition to the analysis on the recuperators, the design of S&T heat exchangers used as PHE is described in this chapter. A MATLAB model based on the method of Bell and Delaware was implemented considering the following assumptions: i) the shell side heat transfer coefficient is modelled according to Fettaka [60], ii) the main geometric assumptions (i.e. baffle spacing, segmental baffle cut ratio or the tube pitch ratio) are taken from Kakaç [61] and iii) a set of typical values of clearances between baffles and tubes and between shell and baffles are taken from Walraven [62], along with the characterization of the tubes layout.

Solar salts are considered as hot fluid (with the thermodynamic and transport properties modelled according to literature [38] as it represents the state-of-the-art in CSP applications: nevertheless, from a qualitative point of view, similar conclusions are expected for the other

Table 10

Assumption on the shell and tube geometry and material.

Parameter	Value
Tube arrangement angle [°]	45
Tube pitch/Tube outer diameter ratio	1.5
Baffle spacing/Shell diameter ratio	0.5
Baffle cut/Shell diameter ratio	0.3
Tube internal roughness [mm]	0.01
Tube material	Inconel 617
Material thermal conductivity [W/m/K] (T in [°C])	$0.0185 \times T + 10.25$
Tube outer diameter (at fixed Tube length/Shell diameter ratio) [mm]	19
Tube thickness [mm]	3.5
Tube length/Shell diameter ratio (at fixed tube diameter)	8

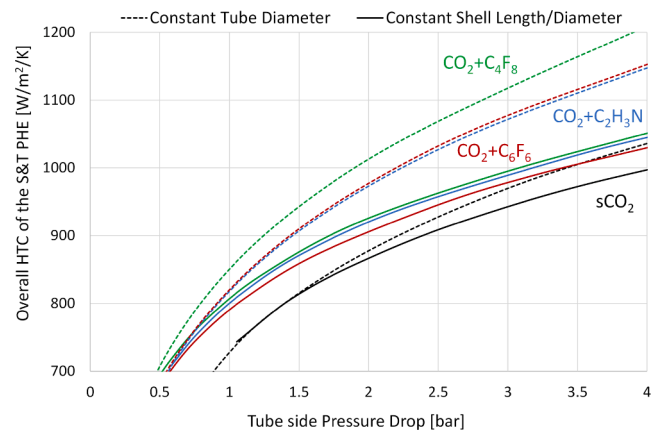


Fig. 10. Dependency of the S&T PHE overall HTC on the pressure drop in the tube side for the simple recuperative cycles working with different CO₂ mixtures and sCO₂. HTC refers to the tube external area.

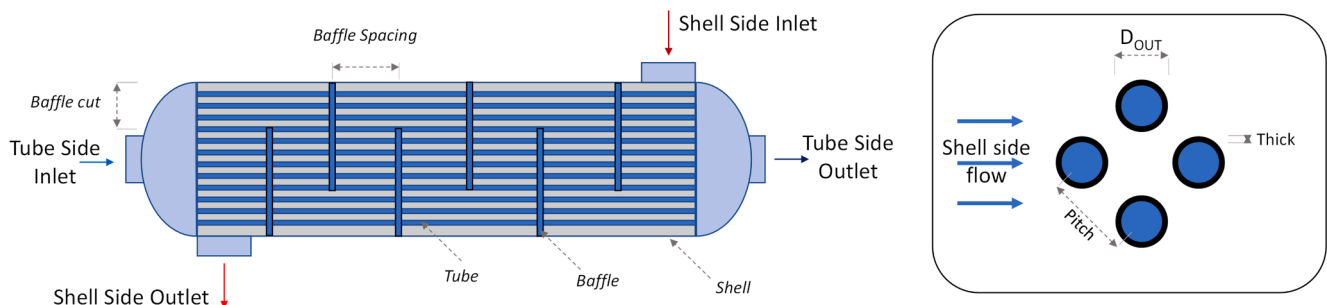


Fig. 9. Shell and tube main geometrical characteristics.

Table 11

Fluid correction factors adopted to correct the literature costs function of the PHE for the mixtures investigated, on the basis of the PHE cost for CO₂.

	CO ₂ + C ₆ F ₆	CO ₂ + C ₂ H ₃ N	CO ₂ + C ₄ F ₈
CO ₂ Molar fraction	84%	85%	73%
HTC variation compared to pure CO ₂ (at constant ΔP)	+12%	+12%	+17%
Fluid Correction Factor for PCHE <i>cost_{fU,PHE,Mix}</i>	0.894	0.894	0.857

Table 12

List of capital cost functions for the various components of the CSP plants.

Component	Cost function	Reference and comments
Heliostats	140 \$/m ²	SAM, [64]. Specific to heliostats area
Concrete solar tower	$C_{ref,tower} \frac{\exp(0.01133 \cdot H_{rec})}{\exp(0.01133 \cdot H_{rec,ref})}$	Turchi, [65]. Actualized to 2020
Receiver	$C_{ref,receiver} \cdot (D \cdot H)^{0.6} + f(Coating) + f(Tubesmass, material)$	Kelly, [39]. Actualized to 2020
HTF piping, HTF pump and HTF other costs	$C_{ref,piping} \left(\frac{Q_{des}}{Q_{des,Ref}} \right)^{0.7}$	Kelly, [39]. Actualized to 2020
TES	$Q_{tes} \cdot V_{HTF} \cdot C_{HTF} + C_{HotTank} + C_{ColdTank} + C_{Other}$	Manzolini, [38]
Cycle Turbine	$0.1826 \cdot W_{turb}^{0.5561} \cdot f_{Temperature}$	Weiland, [58]
Cycle Compressor	$1.23 \cdot W_{compr}^{0.3992}$	Weiland, [58]
Cycle Condenser	$32.88 \cdot UA_{Cond}^{0.75}$	Weiland, [58]
Motor for Compressor	$0.2114 \cdot W_{compr}^{0.6227}$	Weiland, [58]
Generator for Turbine	$0.1089 \cdot W_{turb}^{0.5463}$	Weiland, [58]
Cycle Recuperator	$f_{U,PHE,Mix} \cdot 49.45 \cdot (UA_{PCHE})^{0.7544} \cdot f_T$	Weiland, [58]. Corrected for fluid effects
Cycle PHE	$f_{inst+eng} \cdot f_{U,PHE,Mix} \cdot UA \cdot 2.116 \cdot \Delta P_{Tube}^{-0.2705}$	Thermoflex 29, [63]. Corrected for fluid and material effects. (See Appendix F)

fluids listed in Table 7. In the model proposed, the salts flow in the shell side, while the cycle working fluid at high pressure flows in the tubes. Fig. 9 depicts the adopted single pass S&T geometry on the left, while, on the right, is reported the tube rotates square layout. Table 10 presents the main characteristics of the shell and tube heat exchangers assumed in the MATLAB model, briefly described in Appendix D and used to design the PHE of the power cycles with various working fluids.

The purpose of designing different shell and tubes as PHE of different cycles is analogous to the one proposed for PCHE: at first, the influence of different working fluids on the overall heat transfer coefficient of the HX is determined, including a sensitivity analysis on the pressure drops on the tube side (i.e. the power cycle side). Then, some considerations about the costs of the heat exchangers are drawn. The temperature and pressure range of each shell and tube PHE are reported in Appendix E only for the tube side, as the shell side is assumed ideal liquid, with no influence of the pressure on its properties. The results are reported both assuming the value proposed in Table 10 of the tube length to shell diameter ratio, varying the tube diameter, and assuming value in Table 10 for the tube diameter, varying the tube length to shell diameter ratio. The underlying reason for this approach is to understand whether it is more convenient to increase the tube side pressure losses increasing the tube length or decreasing the tube diameter.

Fig. 10 reports the trends of the heat transfer coefficients for the various configurations of shell and tubes designed, function of the tube

side pressure drops. All the investigated CO₂ mixtures have higher heat transfer performances with respect to the pure sCO₂ in a shell and tubes PHE. From the results it is evident that increasing the tubes length, fixing their diameter, is the most advantageous approach to increment the heat transfer coefficient for these HXs, limiting the increment of the pressure drop.

The qualitative results of the S&T design are different than the ones about the PCHE: regarding the recuperator, the CO₂ + C₄F₈ mixture has the lowest heat transfer coefficient at constant pressure drops, while, when the same mixture is adopted in the shell and tube PHE with solar salts on the shell side, it presents the highest heat transfer coefficient. Comparing the results of the CO₂ + C₄F₈ mixture with sCO₂, the most relevant contribution to the different heat exchange behavior is the density of the mixture (around 90% higher than the one of pure CO₂), reducing the frictional pressure drop significantly, while still experiencing a slightly higher thermal conductivity. The CO₂ + C₆F₆ mixture, on the other hand, presents thermal conductivity and viscosities in line with CO₂, but a density 40% higher. Finally, the CO₂ + C₂H₃N mixture has the same density and a slightly lower viscosity than CO₂, while the higher thermal performances are given by a 20% increment in thermal conductivity.

Finally, considering the results at variable tube length and constant tube diameter (that guarantee the highest HTC at constant pressure drops), the variation in overall HTC of the PHE for the CO₂ mixtures power cycles with respect to the pure sCO₂ configuration is reported in Table 11, along with the fluid correction factor for the shell and tube cost, assuming a unitary scaling exponent of the cost with respect to the UA size parameter, as suggested by Carlson [57].

Moreover, the generic form of the cost function of the PHE for CSP power cycles is reported in Eq. (16): as described in the previous chapter for the PCHE, it is assumed as cost function for pure sCO₂ with the same tube material and tube side pressure drops, along with similar range of duty and UA.

$$C_{PHE,Mix} = f_{U,PHE,Mix} \cdot C_{PHE,CO_2} (f(UA, \Delta P_{Tube}, Material)) \quad (16)$$

No explicit cost correlations on shell and tubes PHE for sCO₂ cycles have been adopted from previous literature works, differently from the PCHE, as no available correlation of S&T capital cost, to the best knowledge of the authors, is able to cover the wide variability of input required (UA size parameter, tube pressure drops and HX materials). In this case, the software Thermoflex [63] is adopted for the purpose, as it allows for a detailed design of sCO₂ shell and tubes PHE and provides the heat exchanger cost.

Two different sets of simulations have been run within Thermoflex according to the characteristics of the S&T assumed in Table 10: one for PHE with heat duties above 100 MW_{th} and another one with heat duties between 10 MW_{th} and 100 MW_{th}. For each set of simulations, the tube side pressure drops are spanned in a wide range varying the tube length and tube diameter, assuming always solar salts on the shell side and pure sCO₂ at 254 bar as working fluid, with a maximum temperature of 550 °C and varying its inlet temperature from 300 °C and 420 °C.

The capital cost function for these HX interpolating the Thermoflex results is reported in Appendix F.

7. Economic analysis

For each of the various solar plant configurations described in this work, two parallel analyses are presented: a technical assessment based on the annual net electric energy yield and an economic analysis, considering the LCOE as economic indicator. These analyses are presented assuming the cycle operating always at full load, when thermal power is available, not considering any dispatching strategy.

The cost functions considered in this work are reported in Table 12: according to the values reported in literature, the higher uncertainties on cost functions are usually related to the solar field and the receiver. For this reason, conservative values on both costs are assumed,

Table 13
Assumptions on the OPEX and financial risk associated to the CSP plant [64].

Assumption	Value
Indirect + Contingency	20% of the CAPEX
Fixed OPEX	66 \$/kW _{el} /year
Variable OPEX	3.5 \$/MWh _{el}
Discount rate	8%
Inflation rate	1%
Plant lifetime	30 years

considering 140 \$/m² of aperture area for the solar field [64] and reference costs from Kelly [39] for the receiver and HTF subsystems, actualized according to the CEPCI index to 2020 and corrected considering a conversion factor of 1.13 \$/€, averaged on the 2020. The solar tower cost is computed assuming a concrete tower with the cost model proposed by Turchi [65]. The TES costs are computed according to a recent work of the authors detailing the characteristics of various storage fluids applied to CSP plants [38], while the power block costs are generally assumed within the cost functions of Weiland [58], being specific for sCO₂ power cycles, except for the correction term applied to the recuperator and the PHE (as described in chapter 6). Other uncertainties are also related to the cost of the HTF to storage medium heat exchanger: as recent studies of Guccione [66,67] detailed this component, the authors implemented analogous cost functions, even if they resulted in an almost negligible solar plant cost share (around 2%).

The other necessary assumptions to move from the capital cost estimation to the LCOE of the CSP plants are presented in Table 13.

The objective of the economic analysis is to properly assess the differences between various plant configurations: while the working fluid selection largely affects the cycle efficiency, hence the yearly energy produced (EE_{year}), the effect of the working fluid on the overall CAPEX

breakdown is less evident, since the solar system costs are independently from the power block layout and the TES. On the other hand, different power cycle layouts using the same working fluids will present different capital costs: for example, the cascade cycle is a simple layout recovering heat from the hot source in a wide temperature range. For these reasons, the lower values of cycle efficiencies would entail a lower yearly energy produced, but at the same time this effect is well balanced by the lower capital cost of both the TES and the power block. The recompression cycle, instead, is expected to produce more electric energy yearly, with significantly higher TES costs, due to the lower HTF temperature difference, and power block costs, due to additional power block components. Finally, as the four different solar fields are considered for three cycle maximum temperatures (550 °C, 625 °C and 700 °C), the effects of increasing the technology level related to the higher temperatures will be evidenced on the resulting LCOE.

The cost of the solar field, tower, receiver and solar subsystems (HTF piping and pump) is defined for each temperature level and storage configuration, and it is shared for any combination of working fluids and power block layout, as introduced in Table 2. Therefore, as it represents more than half of the overall capital cost of the power plant, it is detailed in Table 14 for the four solar fields proposed: the reduction in receiver cost moving from the configuration adopting solar salts as HTF to the ones adopting sodium is evidenced, along with the reduction in solar field costs due to the different thermal power to the receiver at design conditions.

The trade-off between the various effects related to costs (hence complexity) of the solar plants and the actual yearly electricity yield is the main outcome of the techno-economic analysis carried out, which is proposed in the following chapter.

Table 14
Capital cost of the solar systems. The denomination of the fields and receivers refers to the ones proposed in Table 3.

	Direct 550 °C	Indirect 550 °C	Indirect 625 °C	Indirect 700 °C
Heliostats cost [M\$]	174.5	167.6	157.6	153.6
Tower cost [M\$]	23.7	37.4	37.4	37.4
Receiver and HTF subsystems cost [M\$]	82.8	69.1	66.7	66.3
Overall solar system cost [M\$]	281.0	274.1	261.7	257.3

Table 15
Characterization of the optimal cycle sizing and yearly energy analysis of the various configurations of CSP plants adopting the direct 550 °C solar field.

Power Cycle 550 °C Direct Storage	Cycle Power [MW _{el}]	η_{Cycle}	CF	$EE_{gross,Yearly}$ [GWh _{el}]	$EE_{Aux,Yearly}$ [GWh _{el}]	$EE_{net,Yearly}$ [GWh _{el}]	Temperature at PHE inlet [°C]	$\eta_{Thermal,Yearly}$	$\eta_{Sol-EI,Yearly}$	
sCO ₂	Simple	81.4	37.4%	69.7%	521	24	497	384	83.8%	15.4%
	Recompressed	90.4	41.7%	69.5%	578	28	550	418	83.5%	17.0%
	Precompressed	86.8	40.0%	69.5%	555	27	528	409	83.6%	16.4%
	Cascade	77.5	35.5%	71.0%	497	15	482	293	84.4%	14.9%
CO ₂ + C ₆ F ₆	Simple	89.7	41.3%	69.6%	574	27	547	406	83.6%	16.9%
	Recompressed	-	-	-	-	-	-	-	-	-
	Precompressed	91.7	42.2%	69.8%	586	26	561	400	83.7%	17.4%
	Cascade	85.6	39.2%	71.1%	549	15	533	293	84.4%	16.5%
CO ₂ + C ₄ F ₈	Simple	88.8	40.9%	69.5%	568	27	541	408	83.6%	16.8%
	Recompressed	94.2	43.4%	69.5%	602	29	573	425	83.5%	17.8%
	Precompressed	91.3	42.0%	69.7%	584	26	558	405	83.6%	17.3%
	Cascade	84.7	38.8%	71.1%	543	15	528	296	84.3%	16.3%
CO ₂ + C ₂ H ₃ N	Simple	89.6	41.2%	70.2%	573	22	551	364	83.9%	17.1%
	Recompressed	-	-	-	-	-	-	-	-	-
	Precompressed	91.2	41.9%	70.3%	584	22	562	361	83.9%	17.4%
	Cascade	85.7	39.2%	71.1%	550	16	534	293	84.4%	16.5%

Table 16

Characterization of the optimal cycle sizing and yearly energy analysis of the various configurations of CSP plants adopting the indirect 550 °C solar field.

Power Cycle 550 °C Indirect Storage		Cycle Power [MW _{el}]	η_{Cycle}	CF	$EE_{gross,Yearly}$ [GWh _{el}]	$EE_{Aux,Yearly}$ [GWh _{el}]	$EE_{net,Yearly}$ [GWh _{el}]	Temperature at PHE inlet [°C]	$\eta_{Thermal,Yearly}$	$\eta_{sol-El,Yearly}$
sCO ₂	Simple	80.5	37.4%	70.9%	509	10	500	384	87.2%	16.1%
	Recompressed	89.3	41.7%	70.6%	565	12	553	418	86.8%	17.8%
	Precompressed	85.8	40.0%	70.7%	543	11	531	409	86.9%	17.1%
	Cascade	76.9	35.5%	71.5%	488	6	482	293	88.0%	15.5%
CO ₂ + C ₆ F ₆	Simple	88.7	41.3%	70.7%	561	12	549	406	86.9%	17.7%
	Recompressed	–	–	–	–	–	–	–	–	–
	Precompressed	90.6	42.2%	70.8%	574	11	562	400	87.0%	18.1%
	Cascade	84.9	39.2%	71.6%	538	6	532	293	88.0%	17.2%
CO ₂ + C ₄ F ₈	Simple	87.8	40.9%	70.7%	555	12	544	408	86.9%	17.5%
	Recompressed	93.0	43.4%	70.6%	588	13	575	425	86.7%	18.5%
	Precompressed	90.2	42.0%	70.8%	571	11	560	405	87.0%	18.0%
	Cascade	84.0	38.8%	71.6%	533	6	527	296	88.0%	17.0%
CO ₂ + C ₂ H ₃ N	Simple	88.7	41.2%	71.1%	562	9	552	364	87.3%	17.8%
	Recompressed	–	–	–	–	–	–	–	–	–
	Precompressed	90.3	41.9%	71.2%	572	9	563	361	87.4%	18.1%
	Cascade	85.0	39.2%	71.5%	539	7	533	293	88.0%	17.2%

8. Results

8.1. Thermodynamic results

In this chapter the different solar fields, power cycles and TES systems explored are described in terms of annual electricity yield for each configuration, along with the main technical and economic key performance indicators. As already mentioned, the calculations are carried out considering Las Vegas (latitude 36.08°, longitude −115.16°, DNI_y = 2672 kWh/m²/year) as location and using hourly DNI data from SolarPilot. As described in chapter 4, the solar fields are designed at solar noon assuming reference values for the cycle efficiency, solar multiple and receiver thermal efficiency, referring to a cycle power of 100MW_{el}. Nevertheless, the optimal solar multiple is not known in advance: for this reason, a sensitivity analysis on both the solar multiple and the TES size is carried out for each configuration proposed, with the aim of minimizing the LCOE. In addition, as each configuration has a specific receiver thermal efficiency (computed according to Fig. 3), cycle efficiency (computed in Aspen Plus), and auxiliary consumptions (computed as reported in Fig. 4), at fixed solar field the various solutions will present different optimal cycle electric power, lower than 100MW_{el} if the optimal solar multiple is higher than the reference value of 2.4.

The overall yearly analysis proposed is based on an hourly discretization of the time domain: for each timestep the solar field optical efficiency is computed in SolarPilot, considered with the hourly DNI data. Then, the receiver thermal efficiency and the parasitic consumption of the HTF pump are included, along with a simplified TES control system that defocuses the heliostats when the TES is full and the nominal thermal power to the cycle is delivered by the HTF.

The resulting thermodynamic performances of the optimal configuration of power cycles investigated in this work are reported in Table 15 for the solar field adopting solar salts as HTF and direct storage (with a cycle maximum temperature of 550 °C), having a yearly optical efficiency of 53.36%. Table 16 presents the results of the solar field with the indirect storage configuration, sodium as HTF (with 550 °C as cycle maximum temperature) and a yearly optical efficiency of 52.08%. Table 17 shows the same results for the configuration at higher temperature (625 °C of cycle maximum temperature, 53.02% of yearly optical efficiency) and indirect storage with sodium as HTF, while Table 18 the last indirect configuration characterized by a cycle maximum temperature of 700 °C, sodium as HTF and yearly optical efficiency of 52.62%. The mixture CO₂ + C₆F₆ is not explored for maximum temperatures of 700 °C and both the CO₂ + C₄F₈ and CO₂ +

C₂H₃N mixtures are only proposed at 550 °C due to the thermal stability limits of C₆F₆, C₄F₈ and C₂H₃N.

As presented in the next chapter, all power cycle design refers to an optimal SM of 2.8 and an optimal TES size of 12 equivalent hours, as this is the condition that minimizes the LCOE for all the configurations proposed.

According to the results, it is evident that all configurations, at optimal SM and TES size, present a capacity factor in the same range, around 70%. The result is very encouraging and demonstrates that all the proposed solar tower CSP plants can achieve a power production profile close to a baseload plant, particularly in the summer season where the capacity factor is higher than the yearly value.

Regarding the power cycle electric efficiencies, the results evidence significant increments in cycle efficiency for the CO₂ based mixtures with respect to sCO₂ cycle (higher than 3% in absolute value, as an average) for the two simpler power cycle adopting the simple recuperative plant layout and the cascade layout. Cycle efficiency increments with respect to sCO₂ are also evidenced for CO₂ mixture transcritical cycles adopting the precompression and recompression layout, but are more limited, below 2% in absolute value. The resulting cycle performances, then, prove the good characteristics of simpler plant layouts for CSP applications, especially when CO₂ mixtures are adopted. As a matter of fact, the two simpler layouts are characterized by a single compression step across the whole power cycle, that for transcritical cycles occurs in the liquid region. This key characteristic is a significant technological advantage that can favor the innovative transcritical cycles based on CO₂ mixture, on the basis of a simpler design process of the components and on the operation of the power cycle.

The auxiliary yearly energy consumption is relevant for the direct storage configuration in Table 15: excluding the cascade plant layout (as it is a configuration that is design to have a low HTF pump consumption), a comparison between the two configurations at 550 °C of cycle maximum temperature adopting a direct and an indirect storage system (in Table 16) can evidence that as an average around 12 GWh (up to 15 GWh) are saved yearly in HTF pump consumption, a difference already marked in Fig. 4. This energy saved can represent between 2% and 3% of the overall yearly energy produced by the CSP plant and it is only ascribed to the different storage configuration. Moreover, adopting the cascade layout helps in cutting this fraction even more.

The temperature of the working fluid of the power cycle entering in the PHE is reported to evidence the dependence of the thermal efficiency on this key variable. Focusing on the direct storage configuration, a variation of PHE inlet temperature (at its maximum for the

Table 17

Characterization of the optimal cycle sizing and yearly energy analysis of the various configurations of CSP plants adopting the indirect 625 °C solar field.

Power Cycle 625 °C Indirect Storage	Cycle Power [MW _{el}]	η_{Cycle}	CF	$EE_{gross,Yearly}$ [GWh _{el}]	$EE_{Aux,Yearly}$ [GWh _{el}]	$EE_{net,Yearly}$ [GWh _{el}]	Temperature at PHE inlet [°C]	$\eta_{Thermal,Yearly}$	$\eta_{sol-EI,Yearly}$
sCO ₂	Simple	80.1	40.6%	71.0%	509	8	439	85.4%	17.5%
	Recompressed	88.8	45.2%	70.8%	560	9	551	84.9%	19.4%
	Precompressed	85.3	43.3%	70.8%	538	9	530	85.1%	18.6%
CO ₂ + C ₆ F ₆	Cascade	76.2	38.0%	71.6%	483	5	478	87.1%	16.8%
	Simple	87.3	44.4%	70.8%	550	9	541	85.1%	19.0%
	Recompressed	—	—	—	—	—	—	—	—
	Precompressed	90.0	45.7%	70.9%	568	9	559	85.1%	19.6%
	Cascade	84.6	42.5%	71.5%	535	6	530	86.5%	18.6%

Table 18

Characterization of the optimal cycle sizing and yearly energy analysis of the various configurations of CSP plants adopting the indirect 700 °C solar field.

Power Cycle 700 °C Indirect Storage	Cycle Power [MW _{el}]	η_{Cycle}	CF	$EE_{gross,Yearly}$ [GWh _{el}]	$EE_{Aux,Yearly}$ [GWh _{el}]	$EE_{net,Yearly}$ [GWh _{el}]	Temperature at PHE inlet [°C]	$\eta_{Thermal,Yearly}$	$\eta_{sol-EI,Yearly}$
sCO ₂	Simple	86.5	43.7%	70.7%	543	7	536	83.6%	18.4%
	Recompressed	94.4	47.9%	70.5%	592	8	584	83.1%	20.0%
	Precompressed	91.0	45.9%	70.8%	571	7	564	83.6%	19.3%
	Cascade	83.5	41.7%	71.2%	526	5	521	84.9%	17.8%

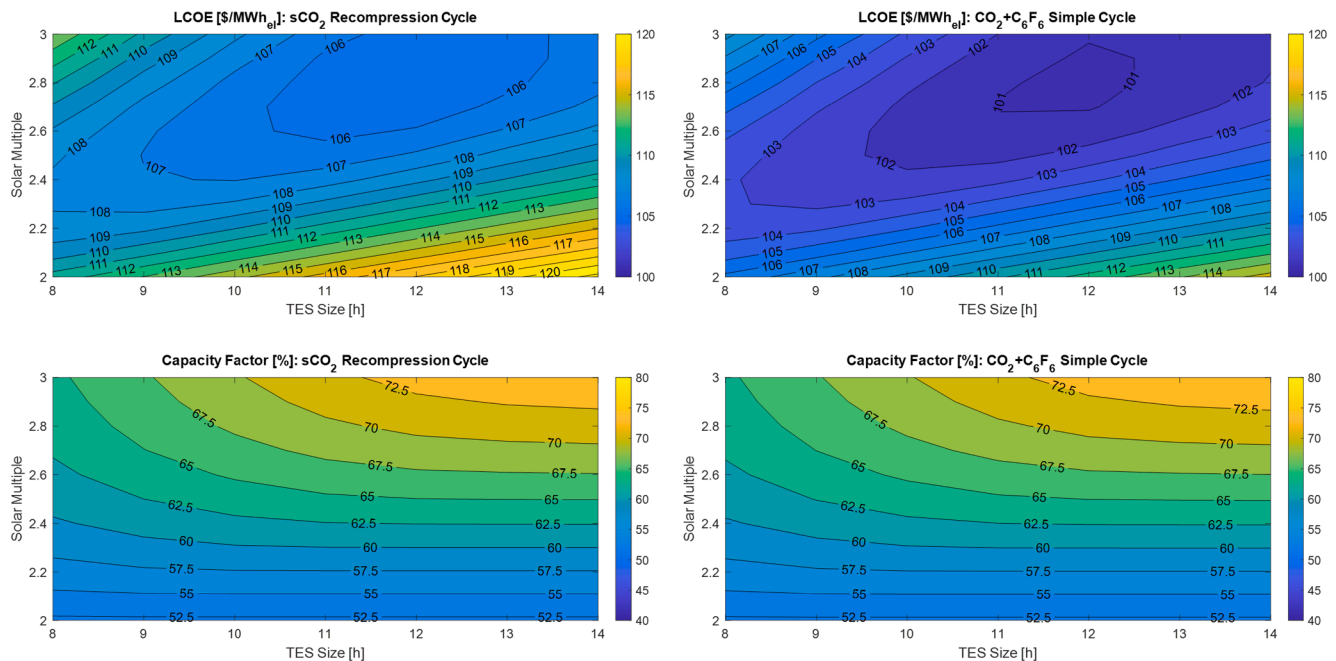


Fig. 11. LCOE and CF maps of the CSP plants with indirect storage and 550 °C of cycle maximum temperature: maps for the sCO₂ recompression cycle (left) and CO₂ + C₆F₆ simple recuperative cycle (right).

recompression cycle and at the minimum for the cascade cycle) justifies a difference in yearly thermal efficiency up to 0.8%, while this difference can be higher than 1% for indirect storage configurations adopting power cycles with the same working fluid and different plant layout. Comparing, instead, the same cycle configuration and working fluid at 550 °C maximum temperature with the direct and the indirect storage, variations in yearly thermal efficiencies can easily reach 3%, depending on the cycle layout and the working fluid, and can be up to 3.6%. Combining the energy saving of the HTF pump and the increment in thermal efficiency of the receiver, this work emphasizes the potentiality of the indirect storage configuration as a possible solution to increase the yearly energy yield of conventional CSP plants. Finally, the yearly values of solar to electric efficiencies varies between 15% and 20%, mainly depending on the maximum temperature levels, as higher cycle

maximum temperatures entail higher cycle efficiencies and therefore higher solar to electric efficiencies.

From the point of view of the net yearly energy produced, the innovative CO₂ based mixtures present non-negligible advantages with respect to sCO₂ cycles, as all power cycle layouts with all the proposed mixtures in this work are able to produce more energy than the sCO₂ counterpart in these CSP plants. This difference is especially evident for the simple recuperative and the cascade layout, where up to 50 GWh_{el} per year (around 10% of the energy produced) are produced with CO₂ based mixtures transcritical cycles more than the energy produced with sCO₂ cycles, under the same conditions. It is crucial to underline that these conclusions are presented fixing the solar field, the receiver and the solar tower between different working fluids, but the optimal power cycle size (its nominal power) results different for each configuration,

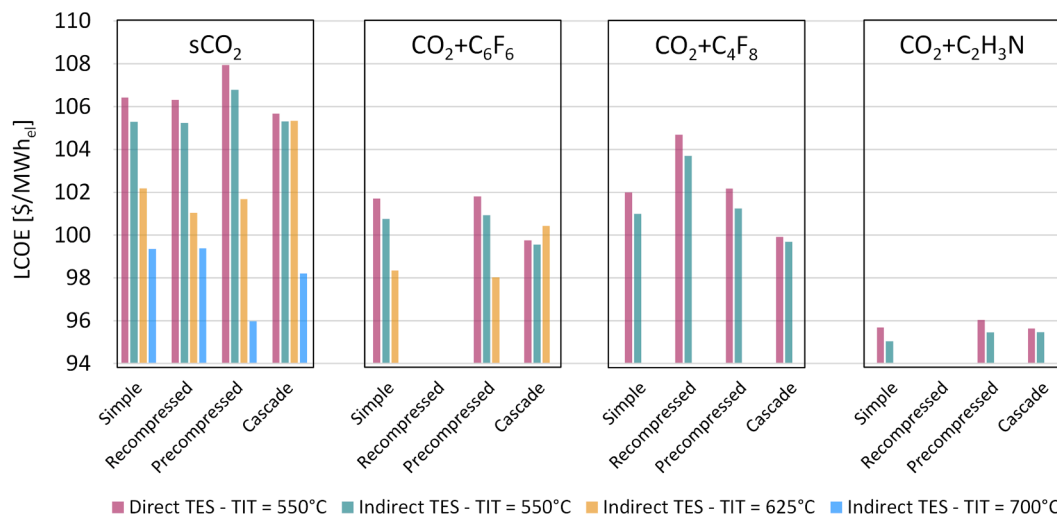


Fig. 12. LCOE of the various configurations of CSP plants studied in this work.

and this directly influences the yearly energy production. The next chapter will investigate the capital cost of each one of the proposed CSP configurations: since the main driver for the development of an innovative technology for power production is the economic competitiveness of the technology itself, a comprehensive analysis including both energetic and economic indicators must be presented and discussed.

8.2. Economic results

For the various configurations of solar plants considered in this work and proposed in the previous chapter, an economic analysis is conducted and presented. The results of the sensitivity analysis of the solar multiple and the TES dimension on the LCOE and the capacity factor are presented in Fig. 11, only for two configurations of cycles at 550 °C maximum temperature and indirect storage system: the recompression sCO₂ cycle (since it is the most studied layout in CSP plants) and the simple recuperative cycle with the CO₂ + C₆F₆ mixture (one of the most studied mixture in the SCARABEUS project, with literature data available on the VLE and thermal stability). These results can be representative of all the calculations carried out within this work, since the other configurations considered present different absolute values of LCOE but identical trends. As already mentioned, and clearly noticeable in the LCOE maps, the condition characterized by a solar multiple of 2.8 and 12 equivalent hours of storage capacity is the optimal and always presents capacity factors around 70%, for this case study. Nevertheless, the results show that profitable configurations are achievable also for a range of capacity factors from 60% (SM of 2.4, 8 h of TES) to 74% (SM of 3, 14 h of TES).

In Appendix G the capital cost breakdown of the many configurations considered in this work is presented, along with the LCOE for each case, where the cost of the solar system has been already detailed in Table 14. The capital cost of the power cycle is evidenced both in specific terms and absolute terms, and it is shown to underline the dependence on the power block costs on the working fluid adopted (to stress the implications of different cost functions of the main heat exchangers, according to the analysis proposed in chapter 6), the cycle maximum temperature and the power cycle layout. The high variability in TES costs stresses the implications of choosing different power cycle layouts on the overall capital costs of the CSP plant: for example, a cost saving in the order of 40 M\$ can be achieved in case the cascade power cycle is adopted with respect to the recompression cycle, representing around 7% of the overall capital cost. The final total cost for each configuration is also reported, including the indirect and contingency additional fraction of the costs: the resulting capital cost specific to the nominal power production capacity is between 5500 and 6300 \$/kW_{el}, depending on the

configuration adopted, a range coherent with values of real power plants with storage capacities in the same range [68]. This result can be compared to other renewable energy technologies, such as PV or wind power, only considering the two inherently advantageous characteristics that CSP proposes with respect to other renewables: the higher capacity factor (around 70% in this work), and the dispatchability of the energy produced.

Finally, the LCOE for each configuration is also proposed, as it is usually considered the key economic indicator for power production technologies, even if its value is normally strongly dependent on the solar resources of the location, on the size of the power plant and on the cost functions adopted. LCOE in the order of 105 \$/MWh_{el} can be achieved in case sCO₂ power cycles are adopted at 550 °C of maximum temperature, while it can easily drop below 100 \$/MWh_{el} if the maximum temperature of the system is moved up to 700 °C. In case CO₂ based mixtures are adopted in transcritical power cycles, the LCOE of the CSP plants is expected to drop with respect to the sCO₂ case by around 5% for the CO₂ + C₆F₆ mixture, 4% for the CO₂ + C₄F₈ mixture and up to 10% in case the CO₂ + C₂H₃N mixture is adopted. As a matter of fact, the CO₂ + C₂H₃N mixture takes the highest advantages from the lower capital cost of the TES systems (given the lower temperature of heat introduction in the power cycles) and the lower capital cost for the main heat exchanger of the power cycles, as reported in chapter 6, while presenting a good cycle efficiency. In addition, the selection of the two complex cycle layouts (the recompression and precompression layout) is not supported by the LCOE as an economic indicator, as the simple recuperative cycle and the cascade cycle presents low LCOE, mainly due to the lower costs of the power block and the TES, which compensate a lower energy production, and can be preferred due to their inherent lower complexity of the power block itself. Finally, all the LCOE of the various configurations considered are reported in Fig. 12.

All the suggested working fluids are able to reach LCOEs below 100 \$/MWh_{el} considering a location with a yearly DNI of 2672 kWh/m²/year: nevertheless, different maximum temperatures (and therefore technological levels) are necessary for this target. The power cycles based on sCO₂ necessitates of cycle maximum temperature around 700 °C, while the innovative CO₂ based mixtures adopted in transcritical cycles can be adopted in the state-of-the-art CSP plants at maximum temperatures around 550 °C.

9. Conclusions

This work presents a techno-economic evaluation of various CSP plants adopting four different power block layouts and four working fluids. sCO₂ as working fluid has been widely adopted in literature as a

reference fluid for power cycles working at 700 °C, especially for CSP applications: nevertheless, the current state-of-the-art of CSP plants considers power cycle maximum temperatures at a level around 550 °C.

From a thermodynamic perspective, the traditional range of cycle minimum temperatures for CSP applications (around 50 °C) are representative of conditions far from the critical point of the pure CO₂, penalizing the compression work and the cycle efficiency of the respective sCO₂ cycle. For these reasons, transcritical cycles adopting CO₂ based mixtures can be a solution to overcome the limit of pure sCO₂ cycles for CSP applications, effectively turning the original supercritical cycle into a transcritical one, increasing the cycle efficiency at the same boundary conditions. Three CO₂ based mixtures are analyzed in this work: the CO₂ + C₆F₆ mixture (already presented in previous works within the SCARABEUS project and experimentally investigated in terms of VLE and thermal stability), the CO₂ + C₄F₈ and CO₂ + C₂H₃N mixtures, which are proposed for the first time as novel working fluids for closed power cycles. For these two mixtures higher uncertainties are presented in terms of experimental data, especially regarding the thermal stability of the dopants. An analysis of the heat transfer characteristics of the innovative mixtures in the two main heat exchangers of the power cycles is carried out adopting finite-volume methods. The results evidenced that different working fluids present different heat exchange performances in similar temperature and pressure ranges: as these conclusions have implications on the cost of the heat exchangers, these effects are preliminary modelled and included in this work.

In addition to the investigation on the innovative working fluids properties, this work proposes a vast sensitivity analysis coupling: working fluids, plant layouts and three maximum temperature levels corresponding to both indirect and direct storage configurations. The four solar plants presented are carefully characterized with dedicated numerical tools at design and off design conditions in terms of their optical efficiency, the receiver thermal efficiency and the auxiliary consumption of the HTF circulation pump. On the basis of an hourly analysis, considering the optical, thermal, power block and auxiliary efficiency characterization of the CSP plant, a yearly assessment of the power conversion from solar to electric is presented assuming Las Vegas as location for the solar plant. In addition, a complete economic analysis is also carried out, for each combination of power block layout, working fluid and maximum temperature level.

The results evidenced the promising techno-economic performances of the innovative mixtures as working fluids in CSP plants, always

superior to the respective sCO₂ configuration at constant cycle maximum temperature, especially in case of indirect storage configurations when sodium is considered as HTF. The simpler power block layouts, characterized by a slightly lower nominal efficiency, have been proved to be highly competitive from an economic point of view with respect to the recompression and the precompression layouts, more investigated in literature for their higher nominal efficiency in CSP applications, and they are suggested for their inherently lower complexity of the power block. In particular the mixture CO₂ + C₆F₆, can allow for a net cycle electric efficiency higher than 42% when coupled with traditional CSP plant exploiting solar salts (with 550 °C of cycle maximum temperature) and presents overall yearly solar to electric efficiencies higher than 17%, with LCOE around 100 \$/MWh_{el} (presenting a 5% reduction with respect to the solution based on sCO₂ cycles). The most cost-effective solution, instead, is the one adopting the CO₂ + C₂H₃N mixture, mainly due to the lower cost related to the power block components and a TES reduced in dimensions, while still holding a good cycle efficiency. As a matter of fact, this solution can theoretically reach LCOE in the range of 95 \$/MWh, 10% lower than the sCO₂ cycle at same temperature levels. For the highest temperature levels on the other hand (with a cycle maximum temperature of 700 °C), the precompressed sCO₂ cycle is suggested as best available option with LCOE around 96 \$/MWh_{el}, due to the high thermal stability of the working fluid itself.

Future works will expand further on the characterization of the design and the off design of the power cycles adopting CO₂ based mixtures in CSP environments, and the economic profitability of solutions including operations at part load will be investigated on the basis of a detailed off design and part load characterizations of the cycles.

Declaration of Competing Interest

The authors declare that they have no known competing financial interests or personal relationships that could have appeared to influence the work reported in this paper.

Acknowledgements

This paper is part of the SCARABEUS project that has received funding from the European Union's Horizon 2020 research and innovation programme under grant agreement No 814985.

Appendix A. Overview of the receiver thermal model and its circuitation

As proposed in Table 4, the receiver thermal model adopts the tube circuitation with two flow paths per receiver, with 4 panels per flow path in the sodium-cooled receiver and 7 panels per flow path for the solar salts-cooled receiver, assumed from literature. The solar plant is located in the northern hemisphere, so the HTF inlet is set in the north-facing panels. A graphical overview of the receiver panels and its circuitation is proposed in Fig. A1.

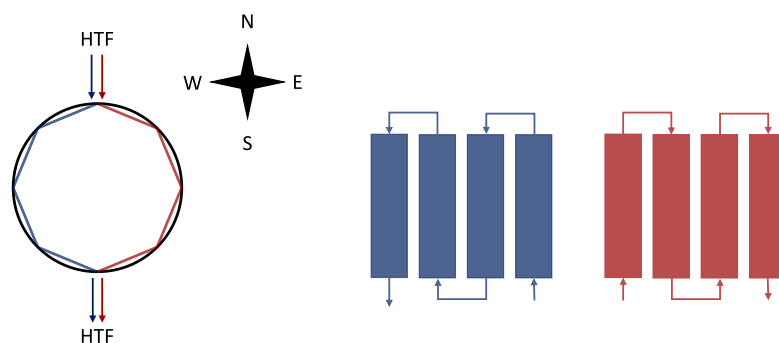


Fig. A1. Planar view of the sodium cooled receiver (left), details of its circuitation (right). The solar salts cooled receiver presents analogous circuitation, but with 7 panels per flow path.

The thermal model adopted is extensively described in literature [47], and it proposes a 2D discretization of the tube domain (along the tube axial and circumferential dimension), where only one tube per panels is modelled (assumed representative of all the tubes in the panels). Along each finite volume, thermal losses are modelled accounting for reflective losses, convective losses (with a simplified model that accounts for the effects of both natural and forced convection), and radiative losses (accounting for the modeling of the view factors). The view factors from each of the finite-volume of the receiver tubes toward the external environment are computed according to the crossed strings method (producing 2D view factors). A more detailed description of the thermal model and its governing equations can be found in the literature describing the adopted model [47].

Appendix B. Transport properties, heat transfer and pressure drop models adopted for the innovative working fluids

While computing the heat transfer coefficients of CO₂ and CO₂ based mixtures, a selection of heat transfer correlations is proposed. For inflow single phase flows the classic Gnielinski correlation has been adopted [69], for flows of condensing mixtures the Cavallini correlation [70] has been adopted, including the Bell and Ghaly [71] correction term for zeotropic mixtures, as suggested by a previous work about experimental validation of heat transfer coefficients of condensing CO₂ mixtures [56]. Moving to the shell side of the shell and tubes heat exchangers, the Bell and Delaware has been developed for the calculation of the shell side convective coefficient, as detailed in Appendix D. Regarding the pressure drop calculations, the classic Darcy–Weisbach equation was adopted for single phase flows and the Del Col correlation for condensing mixtures [72].

In addition, to characterize heat transfer performances of working fluids, accurate models for the transport properties are also implemented. The mixture CO₂ + C₆F₆ is characterized with dedicated MATLAB models, fitted on experimental data of the pure components, already adopted in a previous work dealing with the same mixture [56]. The thermal conductivity of the CO₂ + C₆F₆ mixture is computed with the so-called CO₂-Supertrapp model [73], a modification of the Trapp model that adopts CO₂ as reference fluid instead of octane to improve the matching between the reference fluid and the mixture itself. The same model is also used to compute the viscosities of the vapor phase of the same mixture, while the viscosities of the liquid phase are computed according to the friction theory method of Quiñones-Cisneros [74]. On the other hand, the models for the CO₂ + C₄F₈ and CO₂ + C₂H₃N mixtures have not been modelled in MATLAB on the basis of the pure component characteristics due to lack of experimental data, and the built-in standard TRAPP model has been selected between the ASPEN library as the suggested one for both the viscosity and the thermal conductivity. For pure CO₂, the equation of state implemented in Refprop v10 was adopted in the calculation of transport properties.

Appendix C. Modeling of the PCHE with finite element approach

The heat transfer and pressure drop calculations of the PCHEs are carried out adopting lookup tables for the calculations of all the necessary thermodynamic and transport properties of the working fluid, assuming a fine resolution on temperature (0.5 °C) and pressure (0.5 bar) and interpolating on both variables. The channels are discretized in 500 parts in the axial direction according to a finite volume approach, and for each section on both channels, where the flow is in single phase conditions, the Gnielinski correlation, reported in Eq. (17), has been adopted with the respective friction factor, reported in Eq. (18), while the evaluation of the overall HTC is reported in Eq. (19), assuming no fouling effects. On the other hand, when the flow of the low-pressure channel is in two phase conditions, the Cavallini correlation is adopted to model the heat transfer coefficient of the hot channel, as reported in Appendix B.

$$Nu(i) = \frac{f_{HTC}(i) \cdot (Re(i) - 1000) \cdot Pr(i)}{1 + 12.7 \cdot (Pr(i)^{\frac{1}{4}} - 1) \cdot \sqrt{\frac{f_{HTC}(i)}{8}}} = HTC(i) \cdot \left(\frac{D_{hydr}}{k(i)} \right) \quad (17)$$

$$f_{HTC}(i) = \left(\frac{1}{1.82 \cdot \text{Log}_{10}(Re(i)) - 1.64} \right)^2 \quad (18)$$

$$U(i) = \left(\frac{1}{\frac{1}{HTC_{hot}(i)} + \frac{1}{HTC_{cold}(i)} + \frac{T}{k_{metal}}} \right) \quad (19)$$

Then, the energy balance and the constitutive equation of the HX are solved simultaneously to compute the length of the channel associated to each finite volume, once the mass flow for each channel is set at the desired design value. The pressure drops of the flow in single phase conditions are evaluated adopting the Darcy–Weisbach equation, presented in Eq. (20), and the Chen correlation for the friction factor, reported in Eq. (21), as it has the accuracy of the Colebrook-White correlation, but it is explicit in the friction factor. On the contrary, as for the heat transfer coefficient calculations, when the flow of the low-pressure channel is in two phase conditions the Del Col model is adopted to compute the frictional pressure drop on the hot channel, as mentioned in Appendix B.

$$\Delta P(i) = \frac{f_{DP}(i)}{2} \cdot \frac{L(i)}{D_{hydr}} \cdot \rho(i) \cdot V(i)^2 \quad (20)$$

$$\frac{1}{f_{DP}(i)} = -2 \cdot \text{Log}_{10} \left[\frac{\epsilon}{D_{hydr} \cdot 3.7065} - \frac{5.0452}{Re(i)} \cdot \text{Log}_{10} \left(\frac{1}{2.8257} \cdot \left(\frac{\epsilon}{D_{hydr}} \right)^{1.1098} + \frac{5.8506}{Re(i)^{0.8981}} \right) \right] \quad (21)$$

Appendix D. Modeling of the shell and tubes PHE with finite element approach

In order to design the shell and tube primary heat exchanger in terms of shell diameter, number of tubes, length of the tubes and heat transfer coefficients, the MATLAB model iterates on the shell outer diameter and the length of the shell to fit the required tube side pressure drops with the configuration that minimizes the outer heat transfer surface. The shell and tube geometry is discretized in a number of finite volumes equivalent to the

baffle number. On the tube side, both the pressure drop and the heat transfer coefficient are computed for single phase flows as reported for the PCHE, while the shell side heat transfer coefficient is evaluated with the Bell and Delaware method as reported in literature [60], with the heat transfer coefficient proposed in the Eq. (22):

$$HTC(i)_{Shell} = HTC(i)_{Shell,Ideal} \cdot J_C \cdot J_L \cdot J_B \cdot J_S \cdot J_R \quad (22)$$

All the non-ideality correction coefficients (J_C , J_L , J_B , J_S , J_R) for the definition of the shell side heat transfer coefficient are accurately modelled as suggested by the model on a case specific basis, depending on the tube pitch, tube arrangement, the spacing between the baffles, and other geometrical parameters. Then, the calculation of the overall heat transfer coefficient for each section $U_{ext}(i)$ is computed as in the Eq. (23), relative to the external heat transfer area of the un-finned tubes, excluding fouling factors.

$$U_{ext}(i) = \left(\frac{1}{HTC_{ext}(i)} + \frac{D_{out} \cdot \ln\left(\frac{D_{out}}{D_{in}}\right)}{2 \cdot k_{metal}} + \frac{1}{HTC_{int}(i)} \cdot \frac{D_{out}}{D_{in}} \right)^{-1} \quad (23)$$

Finally, as already done in the design of the PCHE, the energy balance equation and the constitutive equation, reported in Eq. (24), are simultaneously solved to compute the heat exchanged in each finite volume, considering the crossflow mean log temperature correction factor F [60], that allows for the solution of the constitutive equation of a cross flow heat exchanger starting from the simulation of a counter current heat exchanger, proposed in Eq. (25). Tube side pressure drops are computed coherently with the approach developed in the PCHE.

$$U_{ext}(i) = \frac{\dot{Q}(i)}{\Delta T_{ML,CrossFlow}(i) \cdot A_{ext}(i)} \quad (24)$$

$$\Delta T_{ML,CrossFlow}(i) = \Delta T_{ML,CounterCurrent}(i) \cdot F(T_{hot,in}(i), T_{hot,out}(i), T_{coldin}(i), T_{coldout}(i)) \quad (25)$$

Appendix E. Temperature and pressure range for the design of the PCHE and PHE of the simple cycle working with the various working fluids at maximum temperature of 550 °C

Table E1

Temperature and pressure range of the two sides of the PCHE modelled in Fig. 7 for each power cycle considered.

Recuperator (PCHE)	CO ₂ molar fraction	Average HP pressure	Average LP pressure	HP temperature range	LP temperature range
sCO ₂	100%	256 bar	103 bar	112–373 °C	117–439 °C
CO ₂ + C ₆ F ₆	84%	256 bar	80 bar	72–406 °C	91–457 °C
CO ₂ + C ₄ F ₈	73%	256 bar	61 bar	88–408 °C	93–460 °C
CO ₂ + C ₂ H ₃ N	85%	256 bar	88 bar	72–364 °C	87–431 °C

Table E2

Temperature and pressure range of the two sides of the PHE modelled in Fig. 8 for each power cycle considered.

PHE (S&T)	CO ₂ molar fraction	Average Tube side pressure	Shell side temperature range (Solar Salts)	Tube side temperature range
sCO ₂	100%	254 bar	388–565 °C	373–550 °C
CO ₂ + C ₆ F ₆	84%	254 bar	421–565 °C	406–550 °C
CO ₂ + C ₄ F ₈	73%	254 bar	423–565 °C	408–550 °C
CO ₂ + C ₂ H ₃ N	85%	254 bar	379–565 °C	364–550 °C

Appendix F. Cost of the CO₂-solar salts PHE adopting the shell and tube technology modelled in thermoflex

The resulting cost function of the sCO₂ - Solar Salts PHE computed by Thermoflex are graphically reported in Fig. F1: higher tube side pressure drops entail higher velocities, lower heat transfer area and therefore lower capital costs, at constant UA size parameter. The figure also shows the same cost function for large scale PHE according to Carlson [57]: as the Carlson correlation is not dependent on the PHE pressure drop it overestimates (assuming this working fluid, storage fluid and Inconel 617 as tube material), the capital cost of the heat exchanger with respect to the results from Thermoflex, especially at higher tube side pressure drops. The cost correlations adopted in Eq. (16), generated interpolating Thermoflex results, are expressed in the following Eq. (26) and Eq. (27) for two sizes of heat exchangers. Fig. F1 reports Thermoflex results, but in this work the cost function adopted are overestimated by a factor $f_{inst+eng}$ (equal to 2), to move from the capital cost of the materials to the overall cost, including the engineering and installation costs.

$$C_{PHE,CO_2}(f(UA, \Delta P_{Tube}, Material)) [M\$] = f_{inst+eng} \cdot UA \left[\frac{MW}{K} \right] \cdot 2.116 \cdot \Delta P_{Tube} [bar]^{-0.2705} \quad \left(\text{for } Q_{PHE} > 100MW_{th} \right) \quad (26)$$

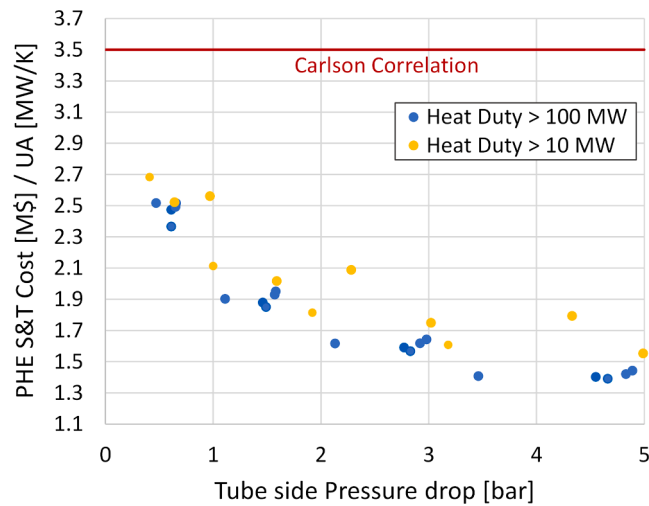


Fig. F1. Cost coefficient computed with Thermoflex 2020 of the shell and tube PHE, as reported in Eq. (16), for the CO₂ - Solar salts configuration assuming Inconel 617 as tube material. In the figure the installation and engineering fraction of the costs are not included.

$$C_{PHE,CO_2}(f(UA, \Delta P_{Tube}, Material)) [M\$] = f_{inst+eng} \cdot UA \left[\frac{MW}{K} \right] \cdot 2.262 \cdot \Delta P_{Tube} [bar]^{-0.2176} \quad \left(\text{for } Q_{PHE} > 10MW_{th} \right) \quad (27)$$

No correction terms have been included in cases the fluid on the shell side is different than solar salts, adopting this cost correlation also in conditions where the cycle maximum temperature is above 550 °C, as the selected material (Inconel 617) is compatible with these conditions.

Appendix G. Capital cost analysis and LCOE of the various configurations of power cycles considered in this work

Table G1
Capital cost analysis and LCOE of the various configurations of power cycles reported in Table 15 adopted to the direct 550 °C solar field.

Power Cycle		Cycle Specific [\$/kW _{el}]	Solar System [M\$]	TES [M\$]	Cycle [M\$]	TOTAL [M\$]	LCOE [\$/MWh _{el}]
550 °C Direct Storage							
sCO ₂	Simple	860	281	71	70	506	106.4
	Recompressed	1086	281	87	98	560	106.3
	Precompressed	1074	281	82	93	547	107.9
	Cascade	1002	281	48	78	488	105.7
CO ₂ + C ₆ F ₆	Simple	879	281	80	79	528	101.7
	Recompressed	-	-	-	-	-	-
	Precompressed	1017	281	78	93	542	101.8
	Cascade	1072	281	48	92	505	99.8
CO ₂ + C ₄ F ₈	Simple	839	281	82	75	525	102.0
	Recompressed	1112	281	92	105	573	104.7
	Precompressed	992	281	80	91	542	102.2
	Cascade	1035	281	49	88	501	99.9
CO ₂ + C ₂ H ₃ N	Simple	757	281	64	68	496	95.7
	Recompressed	-	-	-	-	-	-
	Precompressed	864	281	63	79	508	96.0
	Cascade	835	281	48	72	481	95.6

Table G2

Capital cost analysis and LCOE of the various configurations of power cycles reported in Table 16 adopted to the indirect 550 °C solar field.

Power Cycle 550 °C Indirect Storage		Cycle Specific [\$/kW _{el}]	Solar System [M\$]	TES [M\$]	Cycle [M\$]	TOTAL [M\$]	LCOE [\$/MWh _{el}]
sCO ₂	Simple	861	274	70	69	504	105.3
	Recompressed	1088	274	86	97	557	105.2
	Precompressed	1076	274	81	92	545	106.8
	Cascade	1003	274	48	77	487	105.3
CO ₂ + C ₆ F ₆	Simple	881	274	80	78	526	100.7
	Recompressed	–	–	–	–	–	–
	Precompressed	1020	274	77	92	540	100.9
	Cascade	988	274	48	91	503	99.6
CO ₂ + C ₄ F ₈	Simple	841	274	81	74	522	101.0
	Recompressed	1115	274	91	104	570	103.7
	Precompressed	994	274	79	90	539	101.2
	Cascade	1036	274	48	87	499	99.7
CO ₂ + C ₂ H ₃ N	Simple	758	274	64	67	494	95.0
	Recompressed	–	–	–	–	–	–
	Precompressed	866	274	63	78	505	95.5
	Cascade	836	274	48	71	479	95.5

Table G3

Capital cost analysis and LCOE of the various configurations of power cycles reported in Table 17 adopted to the indirect 625 °C solar field.

Power Cycle 625 °C Indirect Storage		Cycle Specific [\$/kW _{el}]	Solar System [M\$]	TES [M\$]	Cycle [M\$]	TOTAL [M\$]	LCOE [\$/MWh _{el}]
sCO ₂	Simple	821	262	66	66	485	102.2
	Recompressed	1030	262	77	91	529	101.0
	Precompressed	986	262	71	84	513	101.7
	Cascade	1006	262	54	77	483	105.3
CO ₂ + C ₆ F ₆	Simple	847	262	73	74	504	98.4
	Recompressed	–	–	–	–	–	–
	Precompressed	988	262	71	89	518	98.0
	Cascade	1030	262	62	87	506	100.4

Table G4

Capital cost analysis and LCOE of the various configurations of power cycles reported in Table 18 adopted to the indirect 700 °C solar field.

Power Cycle 700 °C Indirect Storage		Cycle Specific [\$/kW _{el}]	Solar System [M\$]	TES [M\$]	Cycle [M\$]	TOTAL [M\$]	LCOE [\$/MWh _{el}]
sCO ₂	Simple	924	257	67	80	505	99.3
	Recompressed	1114	257	79	105	550	99.4
	Precompressed	931	257	66	85	510	96.0
	Cascade	941	257	51	79	484	98.2

References

- Xiao, M., Junne, T., Haas, J., Klein, M., 2021. Plummeting costs of renewables - Are energy scenarios lagging? *Energy Strat. Rev.* 35, 100636. <https://doi.org/10.1016/J.ESR.2021.100636>.
- IEA Report on CSP - 2021 [WWW Document], n.d. URL <https://www.iea.org/reports/concentrated-solar-power-csp> (accessed 7.18.22).
- D. Feldman, M. Bolinger, P. Schwabe, Current and Future Costs of Renewable Energy Project Finance Across Technologies (2020).
- Viebahn, P., et al., 2011. Power tower technology roadmap and cost reduction plan. *Energy Policy* 14, 5–7. <https://doi.org/10.2172/1011644>.
- Vant-Hull, L.L., 2012. Central Tower Concentrating Solar Power (CSP) Systems. *Concentrating Solar Power Technology*, pp. 240–283 <https://doi.org/10.1533/9780857096173.2.240>.
- Fritsch, A., Frantz, C., Uhlig, R., 2019. Techno-economic analysis of solar thermal power plants using liquid sodium as heat transfer fluid. *Sol. Energy* 177, 155–162. <https://doi.org/10.1016/J.SOLENER.2018.10.005>.
- M. Mehos, C. Turchi, J. Vidal, M. Wagner, Z. Ma, C. Ho, W. Kolb, C. Andraka, A. Kruizenga, Concentrating Solar Power Gen3 Demonstration Roadmap. Nrel/Tp-5500-67464, (2017) pp. 1–140. <https://doi.org/10.2172/1338899>.
- White, M.T., Bianchi, G., Chai, L., Tassou, S.A., Sayma, A.I., 2021. Review of supercritical CO₂ technologies and systems for power generation. *Appl. Therm. Eng.* 185 <https://doi.org/10.1016/j.applthermaleng.2020.116447>.
- Neises, T., Turchi, C., 2014. A comparison of supercritical carbon dioxide power cycle configurations with an emphasis on CSP applications. *Energy Procedia* 49, 1187–1196. <https://doi.org/10.1016/J.EGYPRO.2014.03.128>.
- Alfani, D., Neises, T., Astolfi, M., Binotti, M., Silva, P., 2022. Techno-economic analysis of CSP incorporating sCO₂ brayton power cycles: Trade-off between cost and performance. In: AIP Conference Proceedings. AIP Publishing LLC/AIP Publishing, p. 090001. <https://doi.org/10.1063/5.0086353>.
- Binotti, M., Astolfi, M., Campanari, S., Manzolini, G., Silva, P., 2017. Preliminary assessment of sCO₂ cycles for power generation in CSP solar tower plants. *Appl. Energy* 204, 1007–1017. <https://doi.org/10.1016/J.APENERGY.2017.05.121>.
- Crespi, F., Sánchez, D., Rodríguez, J.M., Gavagnin, G., 2017. Fundamental thermo-economic approach to selecting sCO₂ power cycles for CSP applications. *Energy Procedia* 129, 963–970. <https://doi.org/10.1016/J.EGYPRO.2017.09.215>.
- Ahn, Y., Bae, S.J., Kim, M., Cho, S.K., Baik, S., Lee, J.I., Cha, J.E., 2015. Review of supercritical CO₂ power cycle technology and current status of research and development. *Nucl. Eng. Technol.* 47, 647–661. <https://doi.org/10.1016/J.NET.2015.06.009>.
- Rohani, S., Went, J., Duvenhage, D.F., Gerards, R., Wittwer, C., Fluri, T., 2021. Optimization of water management plans for CSP plants through simulation of

- water consumption and cost of treatment based on operational data. *Sol. Energy* 223, 278–292. <https://doi.org/10.1016/J.SOLENER.2021.05.044>.
- [15] Scarabeus H2020 Project [WWW Document], n.d. URL <https://www.scarabeuspr.oject.eu/> (accessed 10.1.21).
- [16] Siddiqui, M.E., 2021. Thermodynamic performance improvement of recompression Brayton cycle utilizing CO₂-C₇H₈ binary mixture. *Mechanics* 27, 259–264. <https://doi.org/10.5755/J02.MECH.28126>.
- [17] Sánchez, C.J.N., da Silva, A.K., 2018. Technical and environmental analysis of transcritical Rankine cycles operating with numerous CO₂ mixtures. *Energy* 142, 180–190. <https://doi.org/10.1016/j.energy.2017.09.120>.
- [18] Shu, G., Yu, Z., Tian, H., Liu, P., Xu, Z., 2018. Potential of the transcritical Rankine cycle using CO₂-based binary zeotropic mixtures for engine's waste heat recovery. *Energy Convers. Manage.* 174, 668–685. <https://doi.org/10.1016/j.enconman.2018.08.069>.
- [19] Astolfi, M., Alfani, D., Lasala, S., Macchi, E., 2018. Comparison between ORC and CO₂ power systems for the exploitation of low-medium temperature heat sources. *Energy* 161, 1250–1261. <https://doi.org/10.1016/J.ENERGY.2018.07.099>.
- [20] Rath, S., Mickoleit, E., Gampe, U., Breitkopf, C., Jäger, A., 2022. Systematic analysis of additives on the performance parameters of sCO₂ cycles and their individual effects on the cycle characteristics. *Energy* 252, 123957. <https://doi.org/10.1016/j.energy.2022.123957>.
- [21] Manzolini, G., Binotti, M., Bonalumi, D., Invernizzi, C., Iora, P., 2019. CO₂ mixtures as innovative working fluid in power cycles applied to solar plants. Techno-economic assessment. *Solar Energy* 181, 530–544. <https://doi.org/10.1016/j.solener.2019.01.015>.
- [22] Binotti, M., Invernizzi, C.M., Iora, P., Manzolini, G., 2019. Dinitrogen tetroxide and carbon dioxide mixtures as working fluids in solar tower plants. *Sol. Energy* 181, 203–213. <https://doi.org/10.1016/J.SOLENER.2019.01.079>.
- [23] Morosini, E., Ayub, A., di Marcoberardino, G., Invernizzi, C.M., Iora, P., Manzolini, G., 2022. Adoption of the CO₂ + SO₂ mixture as working fluid for transcritical cycles: A thermodynamic assessment with optimized equation of state. *Energy Convers. Manage.* 255 <https://doi.org/10.1016/J.ENCONMAN.2022.115263>.
- [24] Crespi, F., Rodríguez de Arriba, P., Sánchez, D., Muñoz, A., 2022. Preliminary investigation on the adoption of CO₂-SO₂ working mixtures in a transcritical Recompression cycle. *Appl. Therm. Eng.* 211 <https://doi.org/10.1016/J.APPLTHERMALENG.2022.118384>.
- [25] Di Marcoberardino, G., Morosini, E., Di Bona, D., Chiesa, P., Invernizzi, C., Iora, P., Manzolini, G., 2022. Experimental characterisation of CO₂ + C₆F₆ mixture: Thermal stability and vapour liquid equilibrium test for its application in transcritical power cycle. *Appl. Therm. Eng.* 212 <https://doi.org/10.1016/J.APPLTHERMALENG.2022.118520>.
- [26] Di Marcoberardino, G., Morosini, E., Manzolini, G., 2022. Preliminary investigation of the influence of equations of state on the performance of CO₂ + C₆F₆ as innovative working fluid in transcritical cycles. *Energy* 238, 121815. <https://doi.org/10.1016/J.ENERGY.2021.121815>.
- [27] Liu, W., Zhang, X., Zhao, N., Shu, C., Zhang, S., Ma, Z., Han, J., 2018. Performance analysis of organic Rankine cycle power generation system for intercooled cycle gas turbine. *Res. Article Adv. Mech. Eng.* 10, 2018. <https://doi.org/10.1177/1687814018794074>.
- [28] Trowbridge, L.D., 2000. Potential Hazards Relating to Pyrolysis of c-C₄F₈O, n-C₄F₁₀ and c-C₄F₈ in Selected Gaseous Diffusion Plant Operations.
- [29] S.C. Moldoveanu, Pyrolysis of Various Derivatives of Carboxylic Acids, in: *Techniques and Instrumentation in Analytical Chemistry*. Elsevier, (2010), pp. 579–627. [https://doi.org/10.1016/S0167-9244\(09\)02819-4](https://doi.org/10.1016/S0167-9244(09)02819-4).
- [30] Kordikowski, A., Schenk, A.P., Van Nielsen, R.M., Peters, C.J., 1995. Volume expansions and vapor-liquid equilibria of binary mixtures of a variety of polar solvents and certain near-critical solvents. *J. Supercrit. Fluids* 8, 205–216. [https://doi.org/10.1016/0896-8446\(95\)90033-0](https://doi.org/10.1016/0896-8446(95)90033-0).
- [31] Byun, H.S., Hasch, B.M., McHugh, M.A., 1996. Phase behavior and modeling of the systems CO₂-acetonitrile and CO₂-acrylic acid. *Fluid Phase Equilib.* 115, 179–192. [https://doi.org/10.1016/0378-3812\(95\)02830-7](https://doi.org/10.1016/0378-3812(95)02830-7).
- [32] Corazza, M.L., Filho, L.C., Antunes, O.A.C., Dariva, C., 2003. High pressure phase equilibria of the related substances in the limonene oxidation in supercritical CO₂. *J. Chem. Eng. Data* 48, 354–358. <https://doi.org/10.1021/JE020150K>.
- [33] Lazzaroni, M.J., Bush, D., Brown, J.S., Eckert, C.A., 2005. High-pressure vapor-liquid equilibria of some carbon dioxide + organic binary systems. *J. Chem. Eng. Data* 50, 60–65. <https://doi.org/10.1021/JE0498560>.
- [34] Dias, A.M.A., Daridon, J.L., Pa, J.C., 2006. Vapor - liquid equilibrium of carbon dioxide - perfluoroalkane mixtures: experimental data and SAFT modeling. *Ind. Eng. Chem. Res.* 45, 2341–2350.
- [35] Span, R., Wagner, W., 1996. A new equation of state for carbon dioxide covering the fluid region from the triple-point temperature to 1100 K at pressures up to 800 MPa. *J. Phys. Chem. Ref. Data* 25, 1509–1596. <https://doi.org/10.1063/1.555991>.
- [36] Manzolini, G., Binotti, M., Morosini, E., Sanchez, D., Crespi, F., Marcoberardino, G. D., Iora, P., Invernizzi, C., 2022. Adoption of CO₂ blended with C₆F₆ as working fluid in CSP plants. In: *AIP Conference Proceedings*. AIP Publishing LLC/AIP Publishing. <https://doi.org/10.1063/5.0086520>.
- [37] Polimeni, S., Binotti, M., Moretti, L., Manzolini, G., 2018. Comparison of sodium and KCl-MgCl₂ as heat transfer fluids in CSP solar tower with sCO₂ power cycles. *Sol. Energy* 162, 510–524. <https://doi.org/10.1016/j.solener.2018.01.046>.
- [38] Manzolini, G., Lucca, G., Binotti, M., Lozza, G., 2021. A two-step procedure for the selection of innovative high temperature heat transfer fluids in solar tower power plants. *Renew. Energy* 177, 807–822. <https://doi.org/10.1016/J.RENENE.2021.05.153>.
- [39] Kelly, B., Izygon, M., Vant-Hull, L., 2010. Advanced Thermal Energy Storage for Central Receivers with Supercritical Coolants. *SolarPaces Conference* <https://doi.org/10.2172/981926>.
- [40] Conroy, T., Collins, M.N., Grimes, R., 2020. A review of steady-state thermal and mechanical modelling on tubular solar receivers. *Renew. Sustain. Energy Rev.* 119, 109591 <https://doi.org/10.1016/J.RSER.2019.109591>.
- [41] Solar Reserve, 2014. Crescent Dunes Solar Energy Plant [WWW Document]. accessed 1.24.23. http://website.eventpower.com/paperclip/exhibitor_docs/15AE/SolarReserve_311.pdf.
- [42] Gentile, G., Picotti, G., Binotti, M., Cholette, M.E., Manzolini, G., 2022. Dynamic thermal analysis and creep-fatigue lifetime assessment of solar tower external receivers. *Sol. Energy* 247, 408–431. <https://doi.org/10.1016/J.SOLENER.2022.10.010>.
- [43] Conroy, T., Collins, M.N., Fisher, J., Grimes, R., 2018. Levelized cost of electricity evaluation of liquid sodium receiver designs through a thermal performance, mechanical reliability, and pressure drop analysis. *Sol. Energy* 166, 472–485. <https://doi.org/10.1016/J.SOLENER.2018.03.003>.
- [44] Asselineau, C.A., Pye, J., Coventry, J., 2022. Exploring efficiency limits for molten-salt and sodium external cylindrical receivers for third-generation concentrating solar power. *Sol. Energy* 240, 354–375. <https://doi.org/10.1016/J.SOLENER.2022.05.001>.
- [45] Steel Tubes, n.d. Dimensions and weights of seamless tubes according to standard ASME B36.10M - Steel tube [WWW Document]. URL <https://www.steeltube.sk/sizes/dimensions-and-weights-of-seamless-tubes-according-to-standard-asm-b36-10m/> (accessed 1.24.23).
- [46] Montoya, A., Rodríguez-Sánchez, M.R., López-Puente, J., Santana, D., 2018. Numerical model of solar external receiver tubes: Influence of mechanical boundary conditions and temperature variation in thermoelastic stresses. *Sol. Energy* 174, 912–922. <https://doi.org/10.1016/J.SOLENER.2018.09.068>.
- [47] Gentile, G., Picotti, G., Casella, F., Binotti, M., Cholette, M.E., Manzolini, G., 2022. SolarReceiver2D: a Modelica package for dynamic thermal modelling of central receiver systems. *IFAC-PapersOnLine* 55, 259–264. <https://doi.org/10.1016/J.IFACOL.2022.09.105>.
- [48] Global Wind Atlas [WWW Document], n.d. URL <https://globalwindatlas.info/> (accessed 7.20.22).
- [49] Idelchik, I.E., Ginevskiy, A.S., Kolesnikov, A.V., Malyavskaya, G.R., Shveyeva, N. K., 2008. *Handbook of Hydraulic Resistance*, 4th Edition. Begell House.
- [50] Alfani, D., Binotti, M., Macchi, E., Silva, P., Astolfi, M., 2021. sCO₂ power plants for waste heat recovery: design optimization and part-load operation strategies. *Appl. Therm. Eng.* 195, 117013 <https://doi.org/10.1016/J.APPLTHERMALENG.2021.117013>.
- [51] Crespi, F., Gavagnin, G., Sánchez, D., Martínez, G.S., 2017. Supercritical carbon dioxide cycles for power generation: A review. *Appl. Energy* 195, 152–183. <https://doi.org/10.1016/j.apenergy.2017.02.048>.
- [52] AspenTech, n.d. Aspen Plus | Leading Process Simulation Software | AspenTech [WWW Document]. URL <https://www.aspentech.com/en/products/engineering/aspen-plus>.
- [53] Morosini, E., Gentile, G., Binotti, M., Manzolini, G., 2022. Techno-economic assessment of small-scale solar tower plants with modular billboard receivers and innovative power cycles. In: *Journal of Physics: Conference Series*. IOP Publishing. <https://doi.org/10.1088/1742-6596/2385/1/012109>.
- [54] Alfani, D., Astolfi, M., Binotti, M., Silva, P., Macchi, E., 2020. Off-design performance of CSP plant based on supercritical CO₂ cycles. *AIP Conf. Proc.* 2303 <https://doi.org/10.1063/5.0029801>.
- [55] Thanganadar, D., Fornarelli, F., Camporeale, S., Asfand, F., Gillard, J., Patchigolla, K., 2022. Thermo-economic analysis, optimisation and systematic integration of supercritical carbon dioxide cycle with sensible heat thermal energy storage for CSP application. *Energy* 238, 121755.
- [56] V. Illyés, E. Morosini, M. Doninelli, X. Guerif, A. Werner, G. di Marcoberardino, G. Manzolini, Design of an air-cooled condenser for CO₂-based mixtures: model development, validation and heat exchange gain with internal microfins, in: *Proceedings of ASME Turbo Expo 2022: Turbomachinery Technical Conference and Exposition*, Volume 9 (2022). <https://doi.org/10.1115/GT2022-82438>.
- [57] M.D. Carlson, B.M. Middleton, C.K. Ho, Techno-economic comparison of solar-driven sCO₂ Brayton cycles using component cost models baselined with vendor data and estimates, in: *Proceedings of the ASME 2017 Power and Energy Conference* 1–7, 2017. <https://doi.org/10.1115/ES2017-3590>.
- [58] N.T. Weiland, B.W. Lance, S.R. Pidaparti, sCO₂ power cycle component cost correlations from DOE data spanning multiple scales and applications, in: *Proceedings of the ASME Turbo Expo*. American Society of Mechanical Engineers (ASME) (2019). <https://doi.org/10.1115/GT2019-90493>.
- [59] V. Dostal, M.J. Driscoll, P. Hejzlar, A Supercritical Carbon Dioxide Cycle for Next Generation Nuclear Reactors. Technical Report MIT-ANP-TR-100 (2004) pp. 1–317. <https://doi.org/10.1016/J.MIT-ANP-TR-100>.
- [60] Fettaka, S., Thibault, J., Gupta, Y., 2013. Design of shell-and-tube heat exchangers using multiobjective optimization. *Int. J. Heat Mass Transf.* 60, 343–354. <https://doi.org/10.1016/J.IJHEATMASSTRANSFER.2012.12.047>.
- [61] Kakaç, S., Liu, H., Pramuanjaroenkij, A., 2020. *Heat Exchangers: Selection, Rating, and Thermal Design*. CRC Press <https://doi.org/10.1201/9780429649862>.
- [62] D. Walraven, Optimization of the Energy Conversion Starting from Low-Temperature Heat: Application to Geothermal Binary Cycles. KU Leuven - Arenberg Doctoral School (2014).
- [63] Thermoform Inc., n.d.
- [64] System Advisor Model [WWW Document], 2020. URL <https://sam.nrel.gov/> (accessed 10.1.20).

- [65] C.S. Turchi, G.A. Heath, 2013. Molten Salt Power Tower Cost Model for the System Advisor Model (SAM).
- [66] Guccione, S., Fontalvo, A., Guedez, R., Pye, J., Savoldi, L., Zanino, R., 2022. Techno-economic optimisation of a sodium–chloride salt heat exchanger for concentrating solar power applications. *Sol. Energy* 239, 252–267. <https://doi.org/10.1016/j.solener.2022.04.052>.
- [67] Guccione, S., 2020. Design and Optimization of a Sodium Molten Salt Heat Exchanger for Concentrating Solar Power Applications. Politecnico di Torino, KTH Royal Institute of Technology.
- [68] C.S. Turchi, M. Boyd, D. Kesseli, P. Kurup, M. Mehos, T. Neises, P. Sharan, M. Wagner, T. Wendelin, 2019. CSP Systems Analysis - Final Project Report.
- [69] Gnielinski, V., 1976. New equations for heat and mass transfer in turbulent pipe and channel flow. *Int. J. Chem. Eng.* 16, 359–368.
- [70] A. Cavallini, D.D. Col, L. Doretti, M. Matkovic, L. Rossetto, C. Zilio, G. Censi, Condensation in horizontal smooth tubes: A new heat transfer model for heat exchanger design. 27 (2006) 31–38. <https://doi.org/10.1080/01457630600793970>.
- [71] Bell, K.J., Ghali, M., 1973. An approximate generalized design method for multicomponent/ partial condensers. *AIChE Symp. Ser.* 69, 72–79.
- [72] del Col, D., Bisetto, A., Bortolato, M., Torresin, D., Rossetto, L., 2013. Experiments and updated model for two phase frictional pressure drop inside minichannels. *Int. J. Heat Mass Transf.* 67, 326–337. <https://doi.org/10.1016/j.jheatmasstransfer.2013.07.093>.
- [73] Ely, J.F., Hanley, H.J.M., 1981. Prediction of transport properties. 1. Viscosity of fluids and 673 mixtures. *Ind. Eng. Chem. Fundam.* 20, 323–332.
- [74] Quiñones-Cisneros, S.E., Zéberg-Mikkelsen, C.K., Stenby, E.H., 2001. One parameter friction theory models for viscosity. *Fluid Phase Equilib.* 178, 1–16. [https://doi.org/10.1016/S0378-3812\(00\)00474-X](https://doi.org/10.1016/S0378-3812(00)00474-X).